Experimental Neurology 323 (2020) 113095

Contents lists available at ScienceDirect

Experimental Neurology

journal homepage: www.elsevier.com/locate/yexnr

Research paper

Helios modulates the maturation of a CA1 neuronal subpopulation required for spatial memory formation

Albert Giralt[a,b,c,d,*], Verónica Brito[b,c,d,e], Monica Pardo[a,b,c,d], Sara E. Rubio[d,f], Lucile Marion-Poll[g,h,i], Raquel Martín-Ibáñez[a,b,c,d], Alfonsa Zamora-Moratalla[j], Carles Bosch[b,d,f], Jesús J. Ballesteros[j], Esther Blasco[k], Aida García-Torralba[l,m], Marta Pascual[b,d,f], Martí Pumarola[k], Jordi Alberch[b,c,d,e,n], Silvia Ginés[b,c,d,e], Eduardo D. Martín[j], Jose Segovia[l,m], Eduardo Soriano[b,d,f,o], Josep M. Canals[a,b,c,d,n,*]

[a] Stem Cell and Regenerative Medicine Laboratory, Department of Biomedical Sciences, Faculty of Medicine and Health Sciences, University of Barcelona, Barcelona, Spain
[b] Neurosciences Institute, University of Barcelona, Barcelona, Spain
[c] Institut d'Investigacions Biomèdiques August Pi i Sunyer (IDIBAPS), Casanova 143, Barcelona, Spain
[d] Centro de Investigación Biomédica en Red sobre Enfermedades Neurodegenerativas (CIBERNED), Spain
[e] Pathophysiology of Neurodegenerative Diseases Laboratory, Department of Biomedical Sciences, Faculty of Medicine and Health Science, University of Barcelona, Barcelona, Spain
[f] Developmental Neurobiology and Regeneration Laboratory, Dept. Cell Biology, Physiology and Immunology, Faculty of Biology, University of Barcelona, Barcelona, Spain
[g] Inserm UMR-S 839, 75005 Paris, France
[h] Sorbonne Université, Faculté des Sciences et d'Ingénierie, 75005 Paris, France
[i] Institut du Fer à Moulin, 75005 Paris, France
[j] Laboratory of Neurophysiology and Synaptic Plasticity, Instituto Cajal, Consejo Superior de investigaciones Científicas, Madrid, Spain
[k] Departament de Medicina i Cirurgia Animals, Universitat Autònoma de Barcelona, Cerdanyola del Vallès, Barcelona, Spain
[l] Division of Hematopoietic Innovative Therapies, Centro de Investigaciones Energéticas, Medioambientales y Technológicas, Centro de Investigación en Red de Enfermedades Raras, Madrid, Spain
[m] Advanced Therapies Unit, Insituto de Investigación Sanitaria Fundación Jiménez Díaz, Madrid, Spain
[n] Production and Validation Center of Advanced Therapies (Creatio), Faculty of Medicine and Health Science, University of Barcelona, Barcelona, Spain
[o] ICREA Academia, Barcelona, Spain

ARTICLE INFO

Keywords:
Long-term potentiation
VSNL1
Hippocampus
Memory
Development
Dendritic spines

ABSTRACT

Currently, molecular, electrophysiological and structural studies delineate several neural subtypes in the hippocampus. However, the precise developmental mechanisms that lead to this diversity are still unknown. Here we show that alterations in a concrete hippocampal neuronal subpopulation during development specifically affect hippocampal-dependent spatial memory. We observed that the genetic deletion of the transcription factor Helios in mice, which is specifically expressed in developing hippocampal calbindin-positive CA1 pyramidal neurons (CB-CA1-PNs), induces adult alterations affecting spatial memory. In the same mice, CA3-CA1 synaptic plasticity and spine density and morphology in adult CB-CA1-PNs were severely compromised. RNAseq experiments in developing hippocampus identified an aberrant increase on the Visinin-like protein 1 (VSNL1) expression in the hippocampi devoid of Helios. This aberrant increase on VSNL1 levels was localized in the CB-CA1-PNs. Normalization of VSNL1 levels in CB-CA1-PNs devoid of Helios rescued their spine loss *in vitro*. Our study identifies a novel and specific developmental molecular pathway involved in the maturation and function of a CA1 pyramidal neuronal subtype.

1. Introduction

Brain circuits show selective connectivities (Brown and Hestrin, 2009; Yoshimura and Callaway, 2005) that might structure information processing and its storage. In particular, the hippocampus is the main nucleus that controls episodic memory, while other nuclei such as the striatum are involved in procedural memory (Morris and Frey, 1997; Packard and Knowlton, 2002). The extent to which individual neurons are interconnected selectively within brain circuits is an unresolved problem in neuroscience. During the recent years, several laboratories

* Corresponding authors at: Department of Biomedical Sciences, Faculty of Medicine and Health Science, University of Barcelona, Barcelona. Spain.
E-mail addresses: albertgiralt@ub.edu (A. Giralt), jmcanals@ub.edu (J.M. Canals).

https://doi.org/10.1016/j.expneurol.2019.113095
Received 19 June 2019; Received in revised form 17 October 2019; Accepted 29 October 2019
Available online 08 November 2019

have elucidated and characterized several subtypes of neuronal types that makes the view of the main tri-synaptic feed forward hippocampal circuit a bit limited. Indeed, distinct research groups have shown the rich variety of neuronal subpopulations in the separate hippocampal subfields, namely CA1, CA2, CA3, CA4 and DG (Cembrowski et al., 2016; Deguchi et al., 2011; Dong et al., 2009; Slomianka et al., 2011; Thompson et al., 2008). The topographic differences are observed from rostral to caudal, from dorsal to ventral and from medial to distal. These differences have been shown by delineating architectonic, morphological, transcriptomic, proteomic and electrophysiological profiles (Cembrowski et al., 2016; Deguchi et al., 2011; Dong et al., 2009; Slomianka et al., 2011; Thompson et al., 2008). To unravel how these specific neuronal subpopulations, develop, mature and establish appropriate connections is even more challenging and in turn, less studied.

The “critical period”, in terms of spinogenesis and neuronal maturation, of the hippocampal development is very sensitive to external/environmental as well as internal/genetic challenges capable to alter the proper connectivity and maturation of the region. Furthermore, it has been shown that such changes cannot be observable until the brain reaches the maturity (Huang et al., 2014; Li et al., 2015). One of the most sensitive processes during hippocampal development is spinogenesis. Dendritic spine number undergoes substantial changes during development, and abnormalities in these processes likely contribute to the pathology of several brain disorders. Spine pathology can affect both neurodevelopmental and neurodegenerative diseases and it is widely thought that these alterations are the intrinsic cause of the accompanying neurological disturbances (Fiala et al., 2002). Some molecules that could be involved with these processes are the calcium sensors like for example the Visinin like-1 (VSNL1) protein. Indeed, mutations in the VNSL1 gene have been linked to hippocampal-related neurological diseases such as Alzheimer's disease and schizophrenia (Braunewell et al., 2011a, 2011b; Hollingworth et al., 2012).

Ikaros and Helios, which are members of the same family, have been described as transcription factors with zinc-finger domains (Cobb and Smale, 2005). We have previously reported the expression of Ikaros (Martin-Ibanez et al., 2010) and Helios (Martin-Ibanez et al., 2012) in the central nervous system. Ikaros expression is mainly detected in the embryonic lateral ganglion eminence (striatum) and postnatal cerebellum (Martin-Ibanez et al., 2010), and its expression is coincident with its role in the development of striatal projecting neurons (Agoston et al., 2007; Martin-Ibanez et al., 2010). Interestingly, Helios has been detected in the hippocampal CA1 and the striatum at embryonic but not adult stages (Martin-Ibanez et al., 2012), which suggests a role for this transcription factor in the developmental regulation of neural systems involved in intellectual functions. In particular, the constricted Helios expression in the CA1 suggests that this transcription factor could play a relevant role in the modulation of cognitive functions dependent on this hippocampal region such as episodic memory (Sellami et al., 2017; Dimsdale-Zucker et al., 2018; Stevenson et al., 2018).

In the present work, we examined how lack of Helios expression affects hippocampal development and mouse behavior during neonatal development and in the adulthood. Our results demonstrated that adult mice devoid of Helios ($He^{-/-}$) display specific hippocampal-related cognitive deficits, whereas neonatal $He^{-/-}$ mice behaved normally. Biochemical and synaptic plasticity experiments carried out in adult $He^{-/-}$ mice demonstrated that Helios has a specific and important role for a correct function of hippocampal calbindin-positive CA1 pyramidal neurons regulating spinogenesis and, furthermore, *in vitro* experiments indicated that Visinin-like protein 1 (VSNL1) could play an important role in such processes.

2. Materials and methods

2.1. Animals

For this study we used wild type ($He^{+/+}$) and *knockout He* ($He^{-/-}$) female mice (Cai et al., 2009) in a C57/BL6 strain background which were generously provided by professor Katia Georgopoulos (Harvard Medical School, USA). Heterozygous mice ($He^{+/-}$) were removed from the study since they were indistinguishable from $He^{+/+}$ mice (data not shown). Mouse genotype was determined from a tail biopsy as described elsewhere (Martin-Ibanez et al., 2012). All mice were housed together in numerical birth order in groups of mixed genotypes (3–5 mice per cage), and data were recorded for analysis by marks in their fingers or tails. The animals were housed in specific pathogen free (SPF) conditions and with access to food and water *ad libitum* in a colony room kept at 19–22 °C and 40–60% humidity, under an inverted 12:12 h light/dark cycle (from 08:00 to 20:00). All animal procedures were approved by local committees [Universitat de Barcelona, CEEA (133/10); Generalitat de Catalunya (DAAM 5712)], in accordance with the European Communities Council Directive (86/609/EU).

2.2. Characterization of neonatal behavior

$He^{+/+}$ and $He^{-/-}$ female pups were assessed using a slightly modified Fox battery to study reflex and sensorimotor ontogeny (Dierssen et al., 2002; Fox, 1965; Venerosi et al., 2001). The tests were conducted during the dark period between 9 AM and 2 PM under dim light conditions. Each subject was tested at approximately the same time of the day from postnatal day P1 to P14 depending on the test. During testing, animals were removed from their home cages and maintained at constant warm temperature by a small electric mat. Body weight and survival rate were also recorded. The following reflexes and responses were scored: Grasping reflex (if the mouse displayed the reflex was quantified as 0 = yes, or 1 = not), righting reflex (seconds that the pup took to rightly place its body after putting it lying face up), cliff drop aversion (seconds that the pup took to remove the forepaws from the cliff and turned away 90° from it), negative geotaxis test (seconds that the pup took to turn 180° and started to climb), clinging and climbing (seconds in which the pup was able to remain in the wire (moving or not), locomotor activity and “pivoting” (number of 2.5 cm^2 squares crossed with the four paws and number of 180° turns respectively).

2.3. SHIRPA assessment

To provide detailed general phenotype assessment, mice were tested using a modified version of the primary screen so-called Phenotype Assessment (SHIRPA) protocol. Briefly, we measured several parameters such as body weight (g) and body length (cm), body position (curved or normal), tremors (present or not), palpebral closure (eyes visible or visually closed), coat appearance (presence or not of piloerection), number of whiskers (present or clearly reduced), defecations (presence of defecations or not), locomotor activity (number of 2.5 cm^2 squares crossed during 30 s), touch escape reflex (animal reacts or not to touching), corneal reflex (presence or not of palpebral closure reflex when touching), biting behavior (animal bites or not a pencil when placing it close to its mouth), vocalization (the mouse screams or not) and muscular strength (animal keeps at least 30 s in a turned wire or not). For further information, the instructions and the full list of parameters analyzed and how are they analyzed are provided by the Medical Council Research Harwell at the website: *http://www.mgu.har.mrc.ac.uk/MGU-welcome.html*.

2.4. Visual placing response and light/dark choice test

The visual placing response was tested in order to evaluate the

function of the visual system (Metz and Schwab, 2004). For the light/dark choice test we used a corridor made of black perspex (40 cm long x 10 cm wide x 20 cm high) with one well-lighted side (w60 W lamp; 1000 lx) and with the other side in darkness (enclosed; 50 lx). We placed mice individually in the well-lighted side, close to the wall, and recorded the latency to reach the dark side. The procedure was carried out for 3 trials with an inter-trial interval of 15 min for each mouse.

2.5. Open field

To check spontaneous locomotor activity and habituation we used the open field (Giralt et al., 2010). Briefly, the apparatus consisted of a white square arena measuring 40 × 40 × 40 cm. Light intensity was ~150 lx throughout the arena. Animals were placed on the arena center and allowed to explore freely for 15 min during three consecutive days. Time in the center and pathlength (cm) were measured as measures of anxiety-like behaviors and locomotor activity respectively. The behavior was recorded using a video camera and analyzed using the Smart Junior software (Panlab, Spain).

2.6. Dark-light paradigm

The dark-light box consisted in a home-made box with two compartments (Giralt et al., 2013; Brito et al., 2014), which were connected by a door (5 cm × 5 cm) located at floor level in the center of the partition (Bourin and Hascoet, 2003). The light compartment (15 × 12 × 25 cm) was white and directly illuminated with light (200 lx), while the dark compartment (12 × 12 × 25 cm) was black and completely enclosed (20 lx). The test was performed in a dimly lighted room. Each animal was initially confined in the dark compartment and allowed to freely explore the apparatus for 5 min. A video camera recorded the animal behavior. Time to step-through for the first time and total time in the bright compartment were the variables evaluated and analyzed using the Smart Junior software (Panlab, Spain).

2.7. Object recognition test

Novel object recognition test (NORT) was used to analyze recognition memory as described previously. The device consisted in a white circular arena with 40 cm diameter and 40 cm high. The light intensity was 100 lx throughout the arena. Mice were first habituated to the arena in the absence of objects (3 days, 15 min/day). On the fourth day, two similar objects were presented to each mouse during 10 min (A'A" condition) after which they were returned to their home cage for 24 h. After that, the animals were placed in the arena where they were tested during 5 min with a familiar and a new object (A'B condition), and then returned to the home cage. Animal behavior was video tracked and analyzed using the Smart Junior software (Panlab, Spain). Exploring behavior was considered when the animal orientated its nose rubbing/touching the object. The object preference was measured as the time exploring each object x 100/time exploring both objects.

2.8. Strategy shifting in a water T-maze

To evaluate the procedural learning and cognitive flexibility in mice we developed a swimming T-maze test as previously described (Van Raamsdonk et al., 2005). In this test, mice were placed in the base of a transparent water-filled T-maze with an escape submerged platform located in the right arm of the maze (T-maze dimensions: arms, 35 × 20 cm; water depth, 10 cm; platform, 8 × 8 cm). The water temperature was maintained at 26 °C ± 1. A black screen surrounded the tank to avoid the vision of distal cues. The time and the first path taken to reach the platform were recorded. The escape platform location was counterbalanced and placed in the right arm for the 50% of mice and in the left arm for the other 50% of mice. Mice received 12 trials divided in 3 blocks of 4 trials. After 12 trials we started a reversal phase in which the platform was switched to the left arm of the T-maze. Then mice received 12 additional trials divided in 3 blocks of 4 trials.

2.9. T-maze spontaneous alternation (T-SAT)

The transparent T-maze apparatus used for the T-SAT was the same used in the *Strategy shifting in a water T-maze* paradigm but without water. In the training trial, one arm was closed (novel arm) and mice were placed in the stem arm of the T (home arm) and allowed to explore this arm and the other available arm (familiar arm) for 10 min, after which they were returned to the home cage. After inter-trial interval of 2 h mice were placed in the stem arm of the T-maze and allowed to freely explore all three arms for 5 min (testing phase). Because the T-maze was made of transparent methacrylate (0.3 cm of thickness), 5 objects of similar size (~20 cm^3) and highly perceptible were situated surrounding the maze at ~15–20 cm outside the walls. The first choice to turn either to the familiar arm or to the new arm (alternation rate, %) and the number of arm entries (number of entries in the new arm*100/total arm entries) were the two parameters evaluated in the testing phase.

2.10. Place and response learning in a T-maze

Using the same transparent T-maze and the same extra-maze visual cues (see 2.9.) we carried out a spatial *vs* response learning protocol as described previously (Lex et al., 2011) in a new cohort of mice to avoid effects of previous experience with the apparatus and procedure. This new cohort of mice was food deprived to 85% of their normal body weight. The food deprivation was initiated 7 days prior to the T-maze experiment. During the entire experimental procedure mice had food accessibility 1.5 h/day (1 h after the experimental session). Then the animals were habituated to the T-maze for a 5 min period. In the training, mice were then placed in the start arm and trained to run to the end of one forced-goal arm during 4 consecutive trials with a 1 min inter-trial interval. A sweet pellet (Bio-serve, Frenchtown, NJ, USA) was placed at the end of this goal-arm (baited-arm). Mice were allowed to collect and eat the sweet pellet and then returned to their home cage. Latencies to reach the pellet were monitored to evaluate learning skills. In the test, animals were placed in the arm opposite to the baited-arm and all arms remained opened. The first arm visited was registered to evaluate the chosen strategy (response strategy: turn left; place strategy: visit the previously baited arm).

2.11. RNA deep sequencing

RNAseq procedures were carried out in collaboration with IMAGIF (Yves sur Yvette, France). Briefly, library preparation was done using the TruSeq mRNA Stranded library prep kit from Illumina following the manufacturer's instructions. Libraries were quality tested using the Bioanalyzer system from Agilent and semi-quantitative PCR. Sequencing was done using the NextSeq500 from Illumina, generating 75 bp single reads (NextSeq 500 High Output Kit 75 cycles). The data were demultiplexed using the distribution of CASAVA software (CASAVA-1.8.2 bcl2fastq2 v2.15.0). The quality of the data was checked with the software FastQC 0.11. Illumina adapters were removed using Cutadapt-1.3, keeping only reads with a minimal length of 10 nucleotides. After Cutadapt step, the data were mapped using bwa-0.7.4 on reference genome mouse mm10. The bam output files were sorted with samtools. The counting of number reads in each exon has been done with HTSeq-count and DESeq2 for the differential analysis. The accession number for the RNA-seq data reported here is GEO: (GSE124641).

2.12. Histopathological analysis

Many tissues and organs samples were collected from $He^{+/+}$ and

$He^{-/-}$ mice at 7 weeks of age. Tissues were fixed by immersion in 10% neutral buffered formalin (NaCl 138 mM, KCl 2.7 mM, KH2PO4 1.2 mM, Na2HPO4 8.1 mM in distilled water) for 48 h, dehydrated and embedded in paraffin for the histopathologic evaluation. Decalcification in 10% formaldehyde, 8% plus formic acid and 1% methanol was done in order to make the bone tissue able to be cut in the microtome. Tissue sections (3 μm) were obtained with a sliding microtome. Dewaxed sections were stained with hematoxylin and eosin for morphological examination.

2.13. Golgi staining and spine counting

For the Golgi-Colonnier staining, adult $He^{+/+}$ and $He^{-/-}$ mice (7-week-old) were perfused with 2% paraformaldehyde - 2% glutaraldehyde in 0.12 M phosphate buffer. Brains were postfixed overnight. Pieces containing the whole hippocampal formation were dissected out and incubated in a dichromate-Colonnier solution (3% $K_2Cr_2O_7$, 5% glutaraldehyde in H_2O) for 5 days at 15 °C. Pieces were then transferred to a 0.75% $AgNO_3$ solution for 3 days. After embedding the pieces in paraffin, 150 μm thick sections were obtained using a vibratome (Leica, VT1000) and subsequently dehydrated. The sections were then mounted onto slides and coverslipped with an Araldite solution. Images were acquired with an upright microscope (Nikon E600; Nikon. Tallahassee, Florida, USA) and processed with ImageJ software (Rasband, W.S., ImageJ, National Institutes of Health, Bethesda, Maryland, USA). The density of dendritic spines was quantified in the stratum radiatum, *i.e.* in the primary side branches of the apical dendrite of pyramidal neurons located in the CA1 area of dorsal hippocampi of Golgi-stained sections from $He^{-/-}$ and $He^{+/+}$ mice (2–4 side branches per neuron; 4–12 neurons per mice; 4 $He^{+/+}$ and 3 $He^{-/-}$ mice per genotype). Spines were quantified at 100× magnification in a 10-μm long segment of the side branch considered.

2.14. Electron microscopy

For the electron microscopy analysis adult, $He^{-/-}$ and $He^{+/+}$ mice (7-week-old) were perfused with 2% glutaraldehyde 2%, paraformaldehyde in fresh 0.12 M phosphate buffer. Brains were postfixed in the same fixative solution overnight. Tissue slices (150 μm thick sections) obtained in a vibratome (Leica VT100) and containing dorsal hippocampi were then incubated with 2% osmium tetroxide, stained with 2% uranyl acetate, dehydrated and embedded in Araldite. Ultrathin sections were collected using a ultramicrotome (Ultracut E Leica) and cut with a diamond knife on formvar-coated slot grids and stained with lead citrate. Electron micrographs depicting an 18.8 μm^2 area were randomly taken in stratum radiatum layer ($n = 41$ micrographs per group). The number of asymmetric (Gray Type 1) synapses per field was calculated.

2.15. DioListic staining and spine counting and morphology analysis

Hippocampal neurons were labeled using the Helios Gene Gun System (Bio-Rad) as previously described (Brito et al., 2014). Briefly, a suspension buffer containing 3 mg of DiI (Molecular Probes, Invitrogen) dissolved in 100 μl of methylene chloride (Sigma-Aldrich) and mixed with 50 mg of tungsten particles (1.7 mm diameter; Bio-Rad) was spread on a glass slide and air-dried. The mixture was resuspended in 3.5 ml distilled water and sonicated. Subsequently, the mixture was drawn into Tefzel tubing (Bio-Rad), and then removed to allow tube drying during 5 min under a nitrogen flow gas. Then, the tube was cut into 13-mm pieces to be used as gene gun cartridges. Dye-coated particles were delivered in the hippocampus using the following protocol. Shooting was performed over 200-μm coronal sections (obtained in a vibratome, Leica VT100) at 80 psi through a membrane filter of 3 μm pore size and 8 × 10 pores/cm^2 (Millipore). Sections were stored at room temperature in PBS for 3 h protected from light and then subjected to immunofluorescence (see below) against calbindin 28 kDa (#300; Swant, Switzerland), incubated with DAPI (#D1306, Invitrogen), and mounted in Mowiol to be analyzed. Spine density counting and morphology analysis was performed only in calbindin 28 kDa positive pyramidal neurons by using the freeware Neuronstudio (Computational Neurobiology and Imaging Center, Icahn School of Medicine at Mount Sinai) as previously described (Jammalamadaka et al., 2013).

2.16. Immunohistochemistry and immunofluorescence

For the immunohistochemistry experiments P0 and P5 pups were used. Animals were deeply anaesthetized and subsequently intracardially perfused with 4% paraformaldehyde in 0.1 M phosphate buffer. The brains were dissected out and cryoprotected with 30% sucrose in PBS with 0.02% sodium azide and frozen in dry-ice cooled isopentane at −80 °C. Coronal sections (30 μm) were obtained. After blocking, sections were incubated overnight with specific goat antibody against Helios (1:50; #sc-9864, Santa Cruz Biotechnology, Santa Cruz, CA, USA). Primary antibody was visualized by sequential incubation with biotinylated secondary antibodies (1:200, Vector Labs, Burlingame, CA, USA) and the streptavidin-peroxidase complex (1:400, Amersham Biosciences, Pittsburgh, PA; USA). The peroxidase reaction was developed with diaminobenzidine (DAB) intensified with nickel ammonium sulfate and cobalt chloride (DAB/Ni-Co), and H_2O_2. The sections were mounted onto gelatinized slides, dehydrated and coverslipped with Eukkit (Panreac).

For double immunofluorescence studies sections from P0 mice were used. Sections were incubated overnight with the specific goat antibody detecting Helios (1:50) combined with one of the following antibodies: mouse anti-MAP2 (1:500; #M1406, Sigma-Aldrich, St. Louis, MO, USA), rabbit anti- calbindin 28 kDa (1:5000; #CB300, Swant Antibodies, Switzerland), rabbit anti-nestin (1:1000; generous gift from S. Hockfield) and mouse anti-Ki67 (1:50; #ab16667; Abcam, Cambridge, UK). After incubation with appropriate fluorescent secondary antibodies, nuclei were stained with 4′,6-diamidino-2-phenylindole (DAPI; Sigma-Aldrich). Images were acquired under an SP5 confocal microscope (Leica Microsystems, Heidelberg, Germany), and processed with ImageJ software.

For single immunofluorescence studies brains were removed at specific developmental stages (from E16.5 to P35), and frozen in dry ice cooled isopentane. Serial coronal cryostat sections (14 μm) were cut on a cryostat, collected on silane-coated slides and frozen at −20 °C. Tissue sections were blocked for 1 h in PBS containing 0.3% Triton X-100 and 1% bovine serum albumin (BSA). Thereafter, they were incubated overnight at 4 °C in PBS containing 0.3% Triton X-100 and 1% BSA with the antibody anti-Helios (1:50; Santa Cruz). After three PBS washes, sections were incubated for 2 h at room temperature with the secondary antibodies Cy3 donkey anti-goat (1:200; from Jackson Immunoresearch Laboratories Inc. Sacramento, California, USA). At the end, tissue sections were counterstained with DAPI. Images were acquired under an SP5 confocal microscope.

2.17. Confocal imaging

DiI-labeled pyramidal neurons from CA1 of the dorsal hippocampus and medium spiny neurons from the dorsal striatum were imaged using a Leica Confocal SP5 with a × 63 oil-immersion objective (digital zoom 5×) as previously described (Brito et al., 2014). *In vitro* confocal imaging were obtained as for common images as well as for spine density and morphology imaging as previously described (Giralt et al., 2017).

2.18. Electrophysiology

Transverse brain slices (400 μm thickness) obtained using a vibratome (Leica, VT1000) were prepared from $He^{+/+}$ and $He^{-/-}$ mice

(7-week-old). Slices were transferred to an immersion recording chamber and superfused (2.5 ml/min) with equilibrated ACSF maintained at constant temperature (34 °C). Evoked fEPSPs were elicited by stimulation of the Schaeffer collateral fibers with an extracellular bipolar tungsten electrode *via* a 2100 isolated pulse stimulator (A-M Systems, Inc., Carlsborg, WA, USA). The stimulation intensity was adjusted to give fEPSP amplitude that was approximately 50% of maximal fEPSP sizes. Long-term potentiation (LTP) was induced by applying 4 trains (1 s at 100 Hz) spaced 20 s, and potentiation was measured for 1 h after LTP induction at 0.1 Hz. Electrophysiological cortico-striatal experiments were performed as described elsewhere (Giralt et al., 2011a). LTP was induced by applying four 1 s, 100 Hz trains delivered every 10 s, and potentiation was measured for 1 h after LTP induction at 0.1 Hz. For each experiment, fEPSP slopes or PS amplitude were expressed as a percentage of average pre-tetanus baseline slope or amplitude values respectively.

2.19. Western blotting

For western blot analysis we first dissected out the dorsal hippocampal region bilaterally from adult (8-week-old) or neonatal (P8) $He^{+/+}$ and $He^{-/-}$ mice. Hippocampal homogenates processing and western blot protocol were carried out as described elsewhere (Giralt et al., 2011a). Immunoblots were probed with the following primary antibodies: VNSL1 (Proteintech, #13919–1-AP, Manchester, UK), anti-GluN2A (Millipore, #AB1555, Darmstadt, Germany), anti-GluN1 (Chemicon, #MAB363, Temecula, CA, USA), anti-GluN2B (Chemicon, #AB1557); anti-PSD-95/SAP-90 (Cell Signaling, #3450S, Leiden, Neetherlands), anti-SynGAP (Affinity BioReagents, #PA1–046, Golden, CO, USA); anti-Chapsyn110 (Alomone Labs, #APZ-002, Jerusalem, Israel), anti-CaM Kinase II (Santa Cruz Biotechnology, #sc-9035 (M-176), Santa Cruz, CA, USA), and anti-GluN3A (was a gift from Dr. Isabel Pérez Otaño, Alicante, Spain). After primary antibody incubation, blots were incubated with anti-mouse or anti-rabbit IgG HRP-conjugated (Promega, Madison, WI, USA) and developed using the ECL Western blotting analysis system (Santa Cruz Biotechnology). A monoclonal anti-β-tubulin antibody (Sigma, #083M4847V) was used to obtain loading controls. The intensity of the optical density of the bands was quantified using the GelPro 3.2 software (Infaimon).

2.20. Hippocampal primary cultures

Hippocampal neurons were prepared at E17 from our Helios (+/+ or −/− pups) colony as described elsewhere (Giralt et al., 2017). At DIV 20–22, cells were transfected (see below) being fixed 72 h later for 10 min with 40 $g\,l^{-1}$ paraformaldehyde in PB 0.2 M for immunostaining. Fixed cells were permeabilized in 1 $ml\,l^{-1}$ Triton X-100 for 10 min and then blocking was performed with 10 $g\,l^{-1}$ BSA in PBS for 1 h. Cells were incubated with mouse monoclonal antibody for calbindin, (1:1000, Swant, Switzerland) at 4 °C overnight. After three washes with PBS, cells were incubated with the corresponding fluorescent secondary antibody Alexa anti-mouse 647 (1:250; ThermoFisher, UK). After washing twice with PBS, the coverslips were mounted with Vectashield (Vector Laboratories Burlingam, UK). Hippocampal neuron staining was observed with a confocal SP5 (see above).

2.21. Construct generation and transfection

Five different shRNA were designed along Visinin-like 1 mRNA, that consist of sense and antisense sequences (19–21 nt in length) separated by a loop structure (TTCAAGAGA) and a 5′ AAAA overhang. Detailed sequences of the shRNAs are described in Fig. 7A. The sequences included additional restriction sites (*Mlu*I in 5′ and *Xho*I –*Cla*I in 3′) to facilitate their cloning into pLVTHM vector (kindly provided by Dr. Trono). Expression of the shRNAs is driven by H1 promoter and mCherry expression, as a marker, is driven by EF1-alpha promoter. For constructs transfection, hippocampal neurons at DIV 21 were transfected using transfectin (Bio-Rad, Hercules, CA, USA) following the manufacturer's instructions and left for 72 h. Cells were co-transfected with a GFP-expressing construct (Giralt et al., 2017) together with a mCherry-shRNA-Scramble or mCherry-shRNA-VSNL1 construct.

2.22. Experimental design and statistical analysis

All data are expressed as mean ± SEM. Statistical analysis were performed by using the unpaired Student's *t*-test (95% confidence), one-way and two-way ANOVA with Tukey as a *post hoc* test. Fisher's exact test, Chi^2 (χ^2) test and logistic regression were also used as appropriate and indicated in the figure legends. Values of $p < .05$ were considered as statistically significant.

All experiments in this study were blinded and randomized. All mice bred for the experiments were used for preplanned experiments and randomized to experimental groups. Visibly sick animals were excluded before data collection and analysis. Data were collected, processed and analyzed randomly. The experimental design and handling of mice were identical across experiments. Littermates were used as controls with multiple litters (3–5) examined per experiments. All mice were bred in the Animal Facility of the Medical School in the University of Barcelona.

3. Results

3.1. Helios is localized in developing calbindin-positive pyramidal neurons of the CA1

Helios has been recently described to be expressed in ectodermal and neuro-ectodermal derived tissues (Martin-Ibanez et al., 2012). To further analyze the expression pattern of this transcription factor in the brain, we performed a broad immunofluorescence characterization at several developmental stages: E14.5, E16.5, E18.5, P2, P7, P15 and P35. We observed that Helios expression is mostly localized in the pyramidal layer of the hippocampal CA1, the striatum and the Purkinje cell layer of the cerebellum (Supplementary Table 1). Within most of these brain areas, Helios presented a dynamic and transient expression pattern starting at embryonic developmental stages (E14.5-E16.5), peaking between E18.5-P3 and disappearing after P15 (Supplementary Table 1). However, in the cerebellum Helios started to be expressed at P7 and lowered its expression by P35, according to the delayed postnatal development of Purkinje cells. A common feature for all the brain regions analyzed was the absence of Helios expression in the adulthood. We next further characterized Helios expression and localization in the hippocampus during development. At E16.5, Helios expression started to be evident in cells of the hippocampal plate of the CA1 (Fig. 1A-B). These Helios-positive cells were negative for both, Ki67 (Fig. 1C) and nestin (Fig. 1D). At P0, Helios immunostaining still labeled cells in the *stratum pyramidale* of CA1 (Fig. 1E-F). In addition, some cells in the subiculum also expressed Helios at this stage (Fig. 1E-F). No Helios expression was observed in either CA3 or DG (Fig. 1B and E), indicating a very specific localization within the hippocampus.

Double immunostaining for MAP2 and Helios at P0 showed that all Helios-immunoreactive cells were immunostained with the neuronal marker MAP2 in the pyramidal layer of CA1 (Fig. 1G). All Helios-positive cells displayed the typical shape of pyramidal-like neurons. To further characterize Helios-positive pyramidal neurons, we used the calbindin-28 kDa (CB) marker. Our results showed that virtually none of the CB-positive neurons in CA1 displaying morphology of interneurons were positive for Helios (Fig. 1H, arrows). Conversely, we could observe that most of the CB-positive cells in the CA1 pyramidal layer co-expressed the Helios protein (Fig. 1H arrowhead). These Helios positive neurons exhibited pyramidal-like shapes. Thus, our data show that Helios is transiently expressed in the CB-positive subpopulation of pyramidal neurons (CB-CA1-PNs) in the CA1 of the hippocampus.

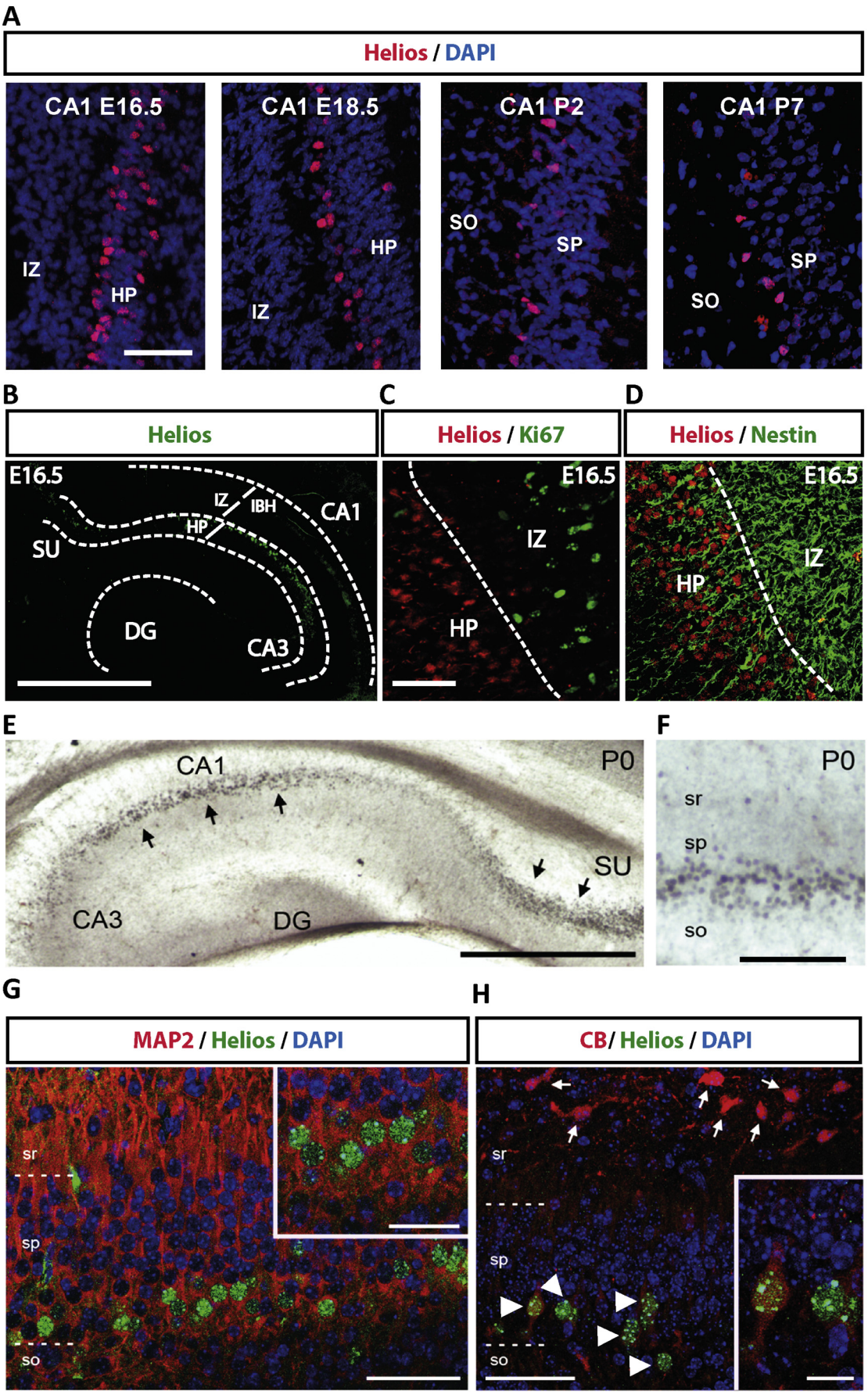

(caption on next page)

Fig. 1. Helios expression pattern localized in the CA1 hippocampal plate/*stratum pyramidale* during development. (A) Double staining for DAPI (blue) and Helios (red) in the hippocampus. From left panel to right panel: embryonic days 16.5 and 18.5 and postnatal days 2 and 7. Scale bar: 70 μm. (B) General view of the Helios expression pattern (green) in the hippocampal formation at embryonic days 16.5. Scale bar: 400 μm. (C) Double staining for Helios (red) and Ki67 (green) in the CA1 at embryonic day 16.5. Scale bar: 40 μm. (D) Double staining for Helios (red) and Nestin (green) in the CA1 at embryonic day 16.5. (E) Immunohistochemistry for Helios (DAB method) in the hippocampal formation at postnatal day 0. Scale bar: 400 μm. (F) Inset of the immunohistochemistry for Helios (DAB method) in the CA1 of the hippocampal formation at postnatal day 0. Scale bar: 70 μm. (G) Double staining for Helios (green) and MAP2 (red) in the CA1 at postnatal day 0. Scale bar: 50 μm. Inset scale bar: 30 μm. (H) Double staining for Helios (green) and calbindin-D28k (red) in the CA1 at postnatal day 0. Scale bar: 50 μm. Scale bar inset: 15 μm. IZ: Intermediate zone; HP: Hippocampal plate; SO: *Stratum oriens*; SP: *Stratum pyramidale*; SR: *Stratum radiatum*; SU: Subiculum; DG: Dentate Gyrus; CA1-CA3: Cornu amonis 1 and 3; IBH: Hippocampal inferior band; CB: Calbindin-D28k. (For interpretation of the references to colour in this figure legend, the reader is referred to the web version of this article.)

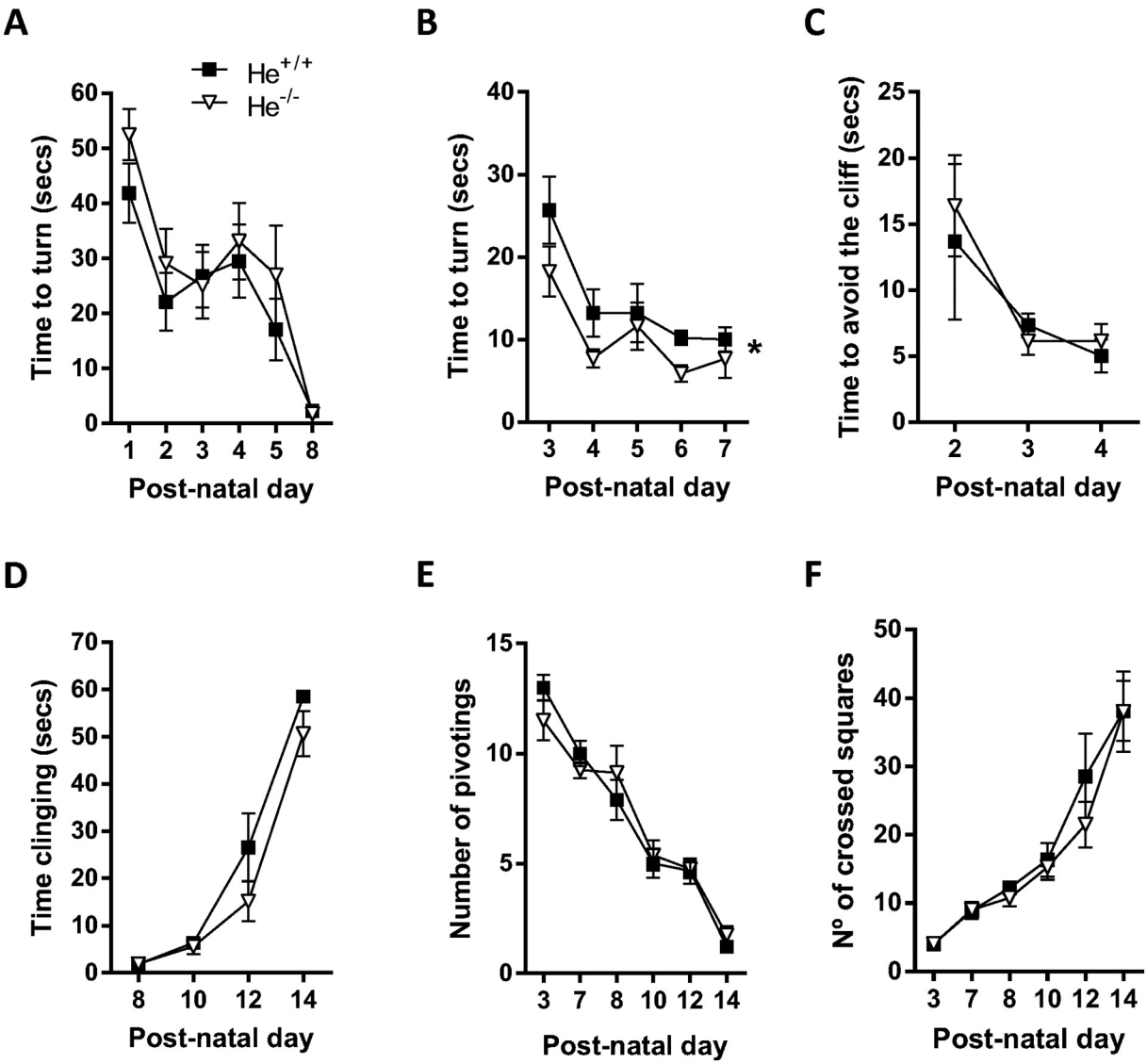

Fig. 2. Neurological and reflexive characterization of $He^{-/-}$ pups during postnatal development. (A) Latencies in the righting reflex test were monitored in $He^{+/+}$ and $He^{-/-}$ pups from P1 to P8 (genotype effect: $F_{(1,\ 15)} = 1.306$, p = n.s.). (B) The latency to show the response to negative geotaxis was evaluated in $He^{+/+}$ and $He^{-/-}$ pups from P1 to P5 (genotype effect: $F_{(1,\ 15)} = 6.614$, $p = .0121$). (C) Aversion to falling from a cliff was checked by measuring the latency to avoid the cliff in $He^{+/+}$ and $He^{-/-}$ pups from P2 to P4 (genotype effect: $F_{(1,\ 15)} = 0.1346$, p = n.s.). (D) Muscular strength and tone were evaluated by the clinging/climbing response and latency to fall from a 90°-placed grid recorded in $He^{+/+}$ and $He^{-/-}$ pups from P8 to P14 (genotype effect: $F_{(1,\ 15)} = 3.362$, p = n.s.). (*E*-F) The development of motor responses and walking maturation were evaluated in an open field (20 cm^2) in $He^{+/+}$ and $He^{-/-}$ pups from P3 to P14. We recorded the number of 2.5 × 2.5 cm crossed squares (E; genotype effect: $F_{(1,\ 15)} = 0.3870$, p = n.s.) and number of 90° pivoting movements (F; genotype effect: $F_{(1,\ 15)} = 0.0013$, p = n.s.). Values are expressed as mean ± SEM. Data was analyzed by two-way ANOVA with repeated measures in all cases. * $p < .05$ as compared to $He^{+/+}$ mice (n = 9 $He^{+/+}$; 8 $He^{-/-}$).

3.2. Normal neurological state in neonatal $He^{-/-}$ mice

In order to study the role of Helios during development a comprehensive neurobehavioral characterization during the postnatal development was carried out in $He^{+/+}$ and $He^{-/-}$ pups. First, $He^{+/+}$ and $He^{-/-}$ pups were able to exhibit a progressive and faster righting reflex response from post-natal day 1 (P1) to post-natal day 8 (P8) without significant differences between genotypes (Fig. 2A). Next, we

evaluated negative geotaxis from P3 to P7. $He^{+/+}$ and $He^{-/-}$ mice were able to elicit a proper progressive and faster response at all ages tested (Fig. 2B). Interestingly, $He^{-/-}$ mice took even shorter time reactions than $He^{+/+}$ mice to show appropriate turning-and-walking behavior in this paradigm (Fig. 2B). In addition, $He^{+/+}$ and $He^{-/-}$ pups were able to successfully demonstrate a cliff aversion response from P2 to P4 (Fig. 2C). We next performed a sensorimotor characterization in pups to check maturation of sensory and motor systems and muscular strength. For the clinging/climbing test, all pups progressively improved the time clinging in the wire mesh from P8 to P14 (Fig. 2D). Additionally, all animals grabbed successfully to the grid (data not shown). Furthermore, the hanging time was not significantly different between $He^{-/-}$ and $He^{+/+}$ mice (Fig. 2D). Pivoting behavior was significantly decreased with age from P3 to P14 (Fig. 2E). In an opposing trend, spontaneous motor activity was significantly increased with age in both genotypes (Fig. 2F), indicating a normal progressive rostro-caudal maturation of the limbs in both, $He^{+/+}$ and $He^{-/-}$ mice. Neither pivoting behavior (Fig. 2E) nor spontaneous locomotor activity (Fig. 2F) were significantly different between genotypes. Altogether indicate that neurological and reflexive behavior in $He^{-/-}$ pups were almost indistinguishable from those on $He^{+/+}$ pups.

3.3. Specific spatial learning and memory deficits in adult $he^{-/-}$ mice

After the broad neonatal characterization, we next performed a comprehensive behavioral characterization in young $He^{+/+}$ and $He^{-/-}$ mice from 5 to 7 weeks of age (See Supplementary fig. 1 for the sequence of the behavioral tests). First, the animals were evaluated by the SHIRPA protocol (at 5 weeks of age) which it gives indications about specific behavioral anomalies resulting from muscular, lower motor neuronal, spinocerebellar, sensory, neuropsychiatric, and autonomic defects. As a result (Supplementary Table 2), $He^{-/-}$ mice showed shorter body length and lower body weight compared to $He^{+/+}$ mice as previously reported (Cai et al., 2009). Additionally, $He^{-/-}$ mice showed less palpebral closure (but normal palpebral reflex) and an absence of startle response compared to $He^{+/+}$ mice (Supplementary Table 2). We further investigated the less palpebral closure as it could affect ulterior behavioral analysis. Necropsy and histological analysis indicated that less palpebral closure in $He^{-/-}$ mice is due to a discrete inflammatory focus near to the sebaceous acini in the tarsal, or in the Meibomian gland in the eyelids (Supplementary Fig. 2A). However, this alteration in the $He^{-/-}$ mice eyelids did not affect either, the retina structure (Supplementary Fig. 2B) or the visual acuity (Supplementary Fig. 2C-D).

Anxiety and locomotor activity and exploration were also evaluated in $He^{+/+}$ and $He^{-/-}$ mice. Anxiety levels were evaluated by using the light-dark paradigm. Both, the total time remaining in the light zone (Supplementary Fig. 2E) and the time to cross from the dark zone to the light zone (Supplementary Fig. 2F) were similar in $He^{+/+}$ and $He^{-/-}$ mice. The comparative exploratory activity from the open field test is shown in (Supplementary Fig. 2G-I). $He^{+/+}$ and $He^{-/-}$ mice did not differ in their first-to-third day covered distance (Supplementary Fig. 2G) or in the time spent in the center (Supplementary Fig. 2H). Furthermore, a similar significant change in activity from day 1 to day 3 was observed in both genotypes regarding to the covered distance (Supplementary Fig. 2G) and center preference (Supplementary Fig. 2H).

Next, we evaluated high cognitive function by carrying out a set of distinct learning and memory paradigms in young (~8 weeks of age) $He^{+/+}$ and $He^{-/-}$ mice. We performed the novel object recognition task (NORT), the T-maze spatial alternation task (T-SAT) and the strategy shifting in a water T-maze involving different dimensions of the mouse cognition. In the NORT, animals were subjected to a training session in the arena in the presence of two similar objects (A and A′). $He^{+/+}$ and $He^{-/-}$ mice similarly explored the object A and A′ indicating no object or place preferences (Fig. 3A). Animals assessed 24 h after training explored with greater preference the new object without significant differences between genotypes, indicating that object recognition memory was not impaired in $He^{-/-}$ mice (Fig. 3A). Next, $He^{+/+}$ and $He^{-/-}$ mice were subjected to the strategy-shifting task in a swimming T-maze (Fig. 3B-C). First, mice were trained to swim to reach the submerged platform located in one arm. In this acquisition phase of the task $He^{+/+}$ and $He^{-/-}$ mice rapidly learned to swim to the platform without significant differences between genotypes, either in the time taken to reach the platform (Fig. 3B), or in the first path to reach the platform (Fig. 3C). Switching the location of the platform to the opposite arm of the maze in the reversal phase revealed no difference between $He^{+/+}$ and $He^{-/-}$ mice either in time taken to reach the platform (Fig. 3B) or in the first path to reach the platform (Fig. 3C). These results indicate that $He^{-/-}$ mice did not display alterations in the strategy shifting ability. In the T-SAT task, spontaneous alternation and arm preference were evaluated 2 h after habituation. We found that $He^{+/+}$ mice significantly alternated whereas $He^{-/-}$ mice did not (Fig. 3D). Furthermore, $He^{+/+}$ mice visited significantly more times the novel arm than the familiar arm whereas $He^{-/-}$ mice showed no preference for any arm (Fig. 3E). Thus, in the T-SAT $He^{-/-}$ mice showed alterations in both variables, spontaneous alternation and new-context exploration. Finally, to evaluate whether $He^{-/-}$ mice display aberrant strategies in the spontaneous alternation in a T-maze, we used a protocol to detect likely aberrant strategies to solve this task (Lex et al., 2011). A new cohort of animals was habituated to the T-maze for a 5 min period with the start arm and one of the lateral arms opened. Both genotypes explored similarly the maze (data not shown). Then, the training procedure started and latencies to collect and eat the sweet pellet placed at the end of the baited arm were similar between groups (data not shown), suggesting similar levels of performance to reach the sweet pellet. Finally, we found that $He^{+/+}$ mice displayed a place learning strategy whereas $He^{-/-}$ mice significantly showed response learning (Fig. 3F). Altogether, these results indicated that spatial learning, but not object recognition memory, procedural learning or cognitive flexibility was affected in $He^{-/-}$ mice.

3.4. Specific impairment of synaptic plasticity in the Schaffer collateral pathway but not in the cortico-striatal pathway in adult $He^{-/-}$ mice

Our results suggested that $He^{-/-}$ mice present cognitive deficits related with hippocampal function, but not with cortico-striatal function. Thus, we next investigated excitatory synaptic transmission and plasticity at Schaffer collateral-CA1 hippocampal synapses and cortico-striatal synapses in slices from 7-week-old $He^{+/+}$ and $He^{-/-}$ mice. First, we analyzed basal synaptic transmission by applying isolated stimuli of increasing intensity to the Schaffer collaterals. For a range of stimulation intensities, the slope of fEPSP responses from $He^{-/-}$ slices was not significantly different from $He^{+/+}$ slices (Fig. 4A, n = 11 slices, 4 mice). Likewise, measurements of the fiber volleys from $He^{-/-}$ and $He^{+/+}$ slices were similar (Fig. 4B, n = 11 slices, 4 mice), and there were no differences in an input/output curve (Fig. 4C). Then, we investigated synaptic plasticity at CA1 hippocampal synapses using a high-frequency conditioning tetanus to induce LTP. Baseline responses were monitored for 10–30 min before conditioning and were found to be stable. $He^{-/-}$ mice showed diminished tetanic conditioning-LTP compared to $He^{+/+}$ animals (Fig. 4D). At 60 min after tetanus, potentiation (as mean percentage of baseline) in $He^{+/+}$ mice was 150.4 ± 8% ($n = 11$ slices) *versus* 121.5 ± 5% in $He^{-/-}$ mice (Fig. 4D; $p < .01$, $n = 12$ slices). Thus, these data represent a possible cellular mechanism for the specific hippocampal-related cognitive deficits observed in $He^{-/-}$ mice.

Next, we examined glutamatergic synaptic transmission in cortico-striatal synapses. Extracellular recordings of population spikes (PS) in acute cortico-striatal brain slices reflect excitatory monosynaptic transmission in a population of striatal neurons due to endogenous glutamate release upon electrical stimulation of glutamate-containing

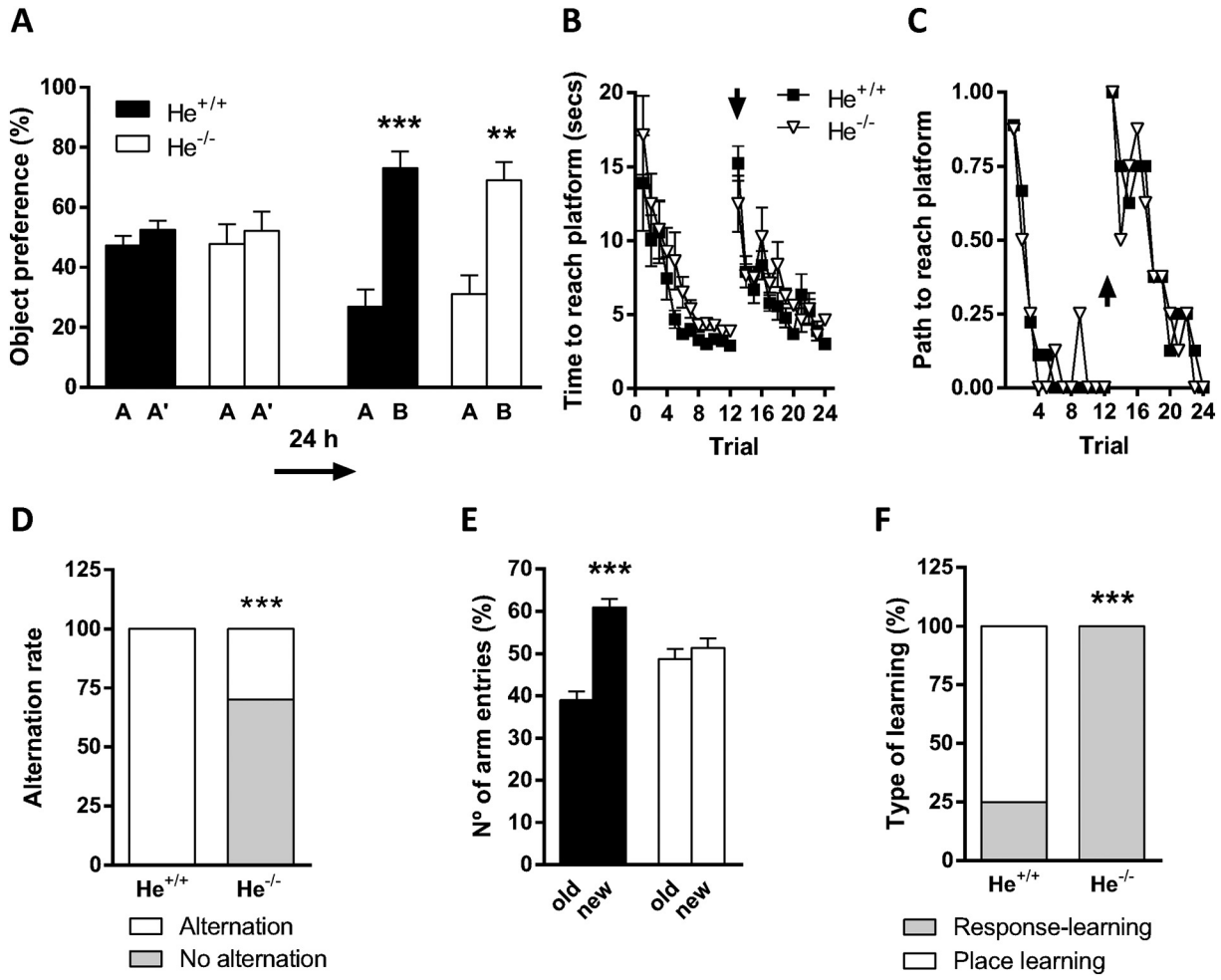

Fig. 3. Specific hippocampal-related learning alterations in $He^{-/-}$ mice. $He^{+/+}$ and $He^{-/-}$ mice at ~8 weeks of age were subjected to different tests of learning of memory. (A) Long-term recognition memory was evaluated in the NORT. Graph shows the percentage of object preference in $He^{+/+}$ and $He^{-/-}$ mice during training and testing (24 h after training; learning effect: $F_{(1,\ 32)} = 50.22$, $p < .001$; genotype effect: $F_{(1,\ 32)} = 2.248e\text{-}005$, $p = .9962$). (B–C) Strategy-shifting capacity was assessed in a swimming T-maze in $He^{+/+}$ and $He^{-/-}$ mice. Latency to reach the platform (B) and path to reach platform (C) were monitored. (D-E) Spatial spontaneous alternation learning was assessed by the T-SAT in $He^{+/+}$ and $He^{-/-}$ mice. Animals were tested for spontaneous alternation rate (D; z = 10.38; $p < .001$) and number of arm entries (E; learning effect: $F_{(1,\ 38)} = 31.56$, $p < .001$; genotype effect: $F_{(1,\ 38)} = 19.65$, $p < .001$) 2 h after the training trial. (F) Place-*vs* Response-learning were tested in a new set of $He^{+/+}$ and $He^{-/-}$ mice in the same T-maze apparatus (z = 10.95; $p < .001$). Bars represent mean ± SEM. Data were analyzed by one-way ANOVA with Tukey's *t*-test as a *post hoc* (A and E), by the Chi-square (χ^2) test (D and F), by two-way ANOVA with repeated measures (B) and by logistic regression with the Wald test as a *post hoc* (C). In A and E: ** $p < .01$, *** $p < .001$ when compared to time exploring object A / number of visits of the old arm. In D and F: *** $p < .001$ when compared to $He^{+/+}$ mice. n = 9 $He^{+/+}$ and 8 $He^{-/-}$ in A-C; $n = 12$ $He^{+/+}$ and 9 $He^{-/-}$ in D and E; $n = 8$/genotype in F.

fibers. We analyzed basal synaptic transmission by applying isolated stimuli of increasing intensity. Extracellular field recordings showed that amplitude of PS responses in $He^{-/-}$ mice was not significantly different from PS response in $He^{+/+}$ mice (Fig. 4E). Finally, we also investigated cortico-striatal synaptic plasticity by inducing LTP by high-frequency conditioning tetanus. Baseline responses were monitored for 10 min before conditioning and were found to be stable. Tetanus conditioning revealed a similar ability to support LTP in $He^{-/-}$ and $He^{+/+}$ mice (Fig. 4F). Taken together, these data indicate that there is a strong correlation between the specific hippocampal-dependent cognitive deficits observed in Fig. 3 and the specific impairments on hippocampal CA3-CA1 LTP.

3.5. Helios deficiency induces specific dendritic spine density and morphology alterations in calbindin-positive CA1 pyramidal neurons

We next evaluated whether hippocampal architecture correlated with above described hippocampal-related cognitive impairments. First, stereological analysis revealed that adult (7–8-week-old) $He^{-/-}$ and $He^{+/+}$ mice have similar hippocampal volume (Supplementary Fig. 3A-B) and density of CA1 pyramidal cells (Supplementary Fig. 3C). Our next goal was to evaluate possible microstructural changes by analyzing neuronal morphology and by counting dendritic spines and synaptic contacts in the *stratum radiatum* of the CA1 in adult $He^{-/-}$ and $He^{+/+}$ mice. We only analyzed symmetric synapses and dendritic spines because Helios is specifically expressed in a subset of pyramidal neurons of the CA1 and because these micro-structures have been more widely characterized in the literature about the modulation of LTP and spatial memory than symmetric/inhibitory synapses (Bourne and Harris, 2011). First, we performed a Golgi staining and observed no gross changes in morphology of CA1-pyramidal neurons in $He^{-/-}$ mice compared to $He^{+/+}$ mice (Supplementary Fig. 3D). Subsequent dendritic spine quantification in 2nd-order apical dendrites from the CA1 pyramidal neurons (localized in the *stratum radiatum*) showed no significant differences in the number of these structures in $He^{-/-}$ mice compared to $He^{+/+}$ mice (Supplementary Fig. 3E-F). We also quantified the density of excitatory synapses in the *stratum radiatum* by electron microscopy, but no significant changes were detected between

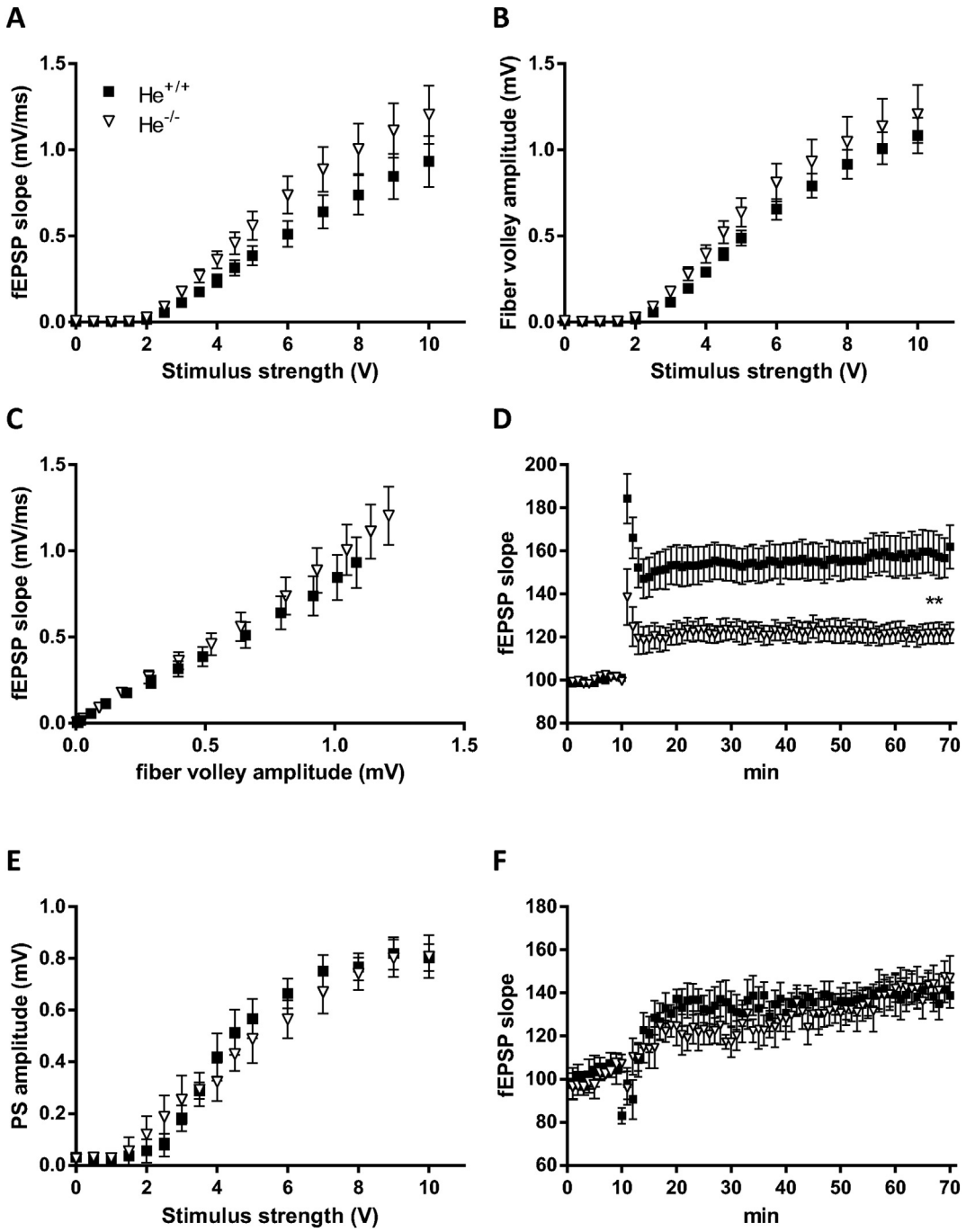

Fig. 4. Characterization of basal synaptic function and synaptic plasticity in cortico-striatal and CA3-CA1 pathways in $He^{-/-}$ mice. (A) Hippocampal field excitatory postsynaptic potential (fEPSP) slopes in 7-week-old $He^{+/+}$ (n = 11 slices) and $He^{-/-}$ (n = 11 slices) mice for a given range of stimulus intensities. (B) Fiber volley amplitudes in hippocampal slices from $He^{+/+}$ (n = 11 slices) and $He^{-/-}$ (n = 11 slices) mice for a given range of stimulus intensities. (C) Input/output relationships for hippocampal slices from $He^{+/+}$ (n = 11 slices) and $He^{-/-}$ (n = 9 slices) mice. (D) Summary data showing the time course of mean fEPSPs slope in $He^{+/+}$ (n = 11) and $He^{-/-}$ (n = 12) mice in basal condition and following hippocampal Schaffer-collateral LTP induction. (E) Population spike (PS) amplitudes for a given range of stimulus intensities are shown from $He^{+/+}$ (n = 13) and $He^{-/-}$ (n = 9) cortico-striatal slices. (F) Summary data showing the time course of mean PS amplitude in cortico-striatal slices from $He^{+/+}$ (n = 7) and $He^{-/-}$ (n = 6) mice in basal condition (10 min) and following LTP induction (60 min). Data were normalized for each slice with respect to the average slope recorded during baseline. Bars represent mean ± SEM. For statistical analysis two-way ANOVA was used. ** $p < .01$ with respect to $He^{+/+}$ mice.

genotypes (Supplementary Fig. 3G-H).

We then hypothesized that, since Helios is expressed only in calbindin-positive pyramidal CA1 neurons during hippocampal development, it is conceivably that specific and localized architectural changes could be found only in this neuronal subtype. Thus, we combined a DiOlistic labeling (Dil) with immunofluorescence against calbindin 1 in fixed hippocampal slices from adult (8-week-old) $He^{+/+}$ and $He^{-/-}$ mice. We then counted dendritic spine density only in double labeled (Dil / Calbindin) neurons from the CA1 pyramidal layer (Fig. 5A-B). We observed that spine density in apical dendrites of CB-positive CA1 pyramidal neurons were decreased in $He^{-/-}$ mice compared to $He^{+/+}$ mice (Fig. 5B-C). Further morphological analysis indicated that specifically thin-like spines were the ones that were significantly reduced (Fig. 5D). As a control, we counted CB-positive CA1 pyramidal cell

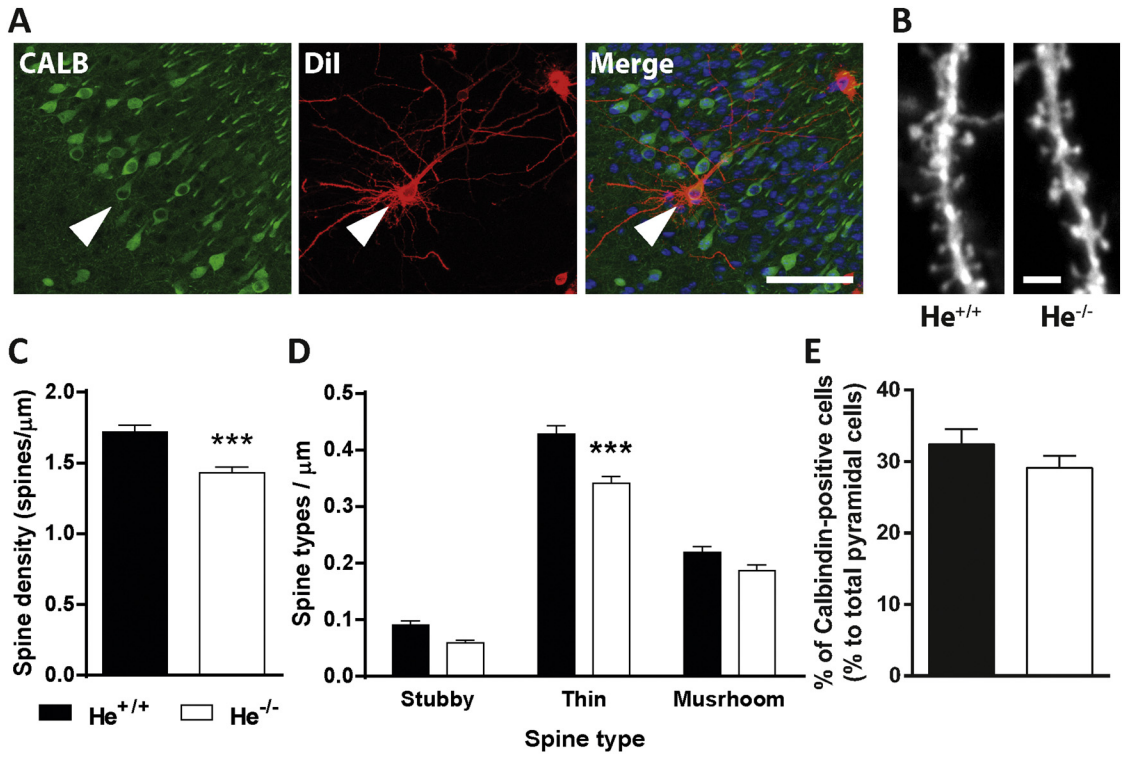

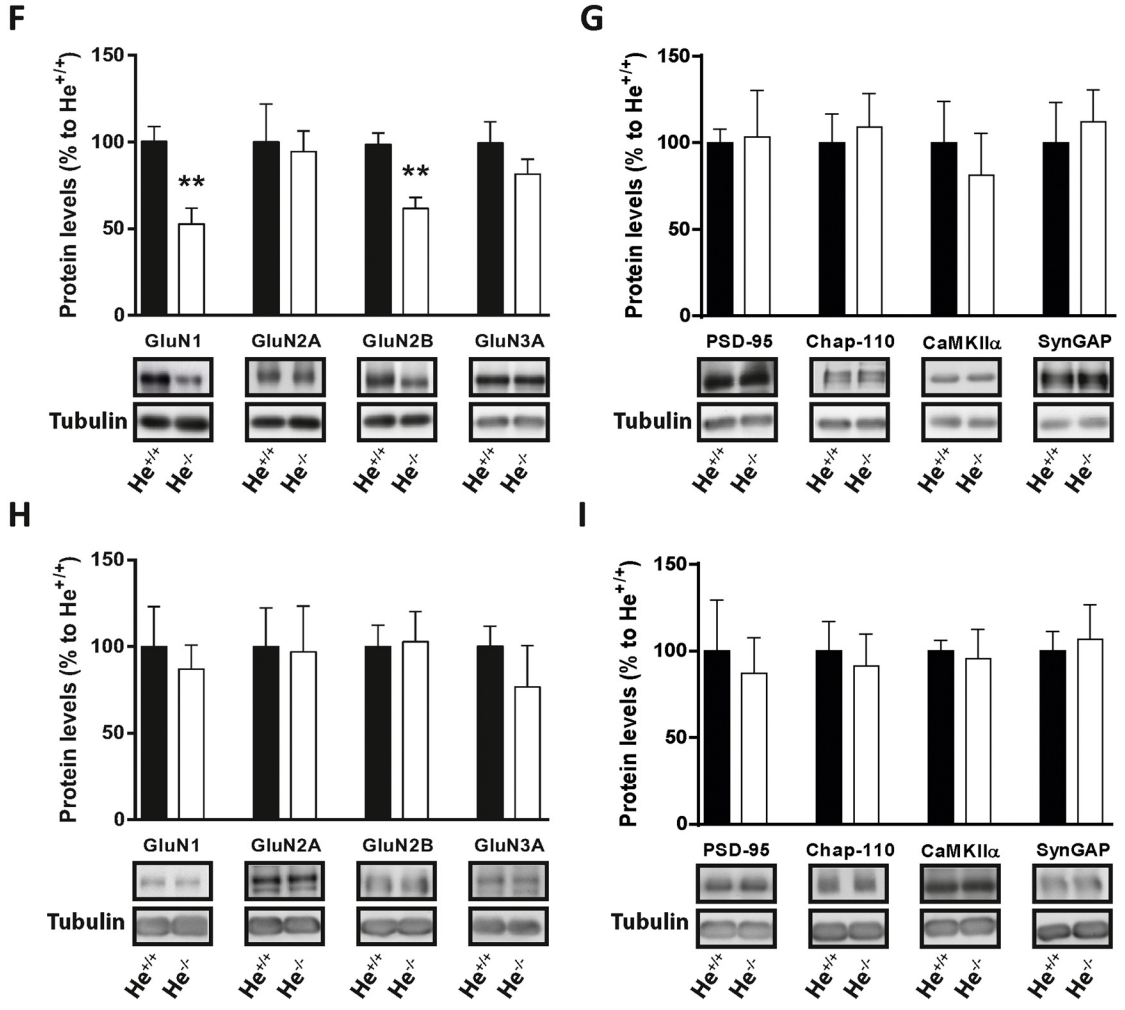

(caption on next page)

Fig. 5. Characterization of structural and biochemical synaptic properties in $He^{+/+}$ and $He^{-/-}$ mice. (A) Confocal microscopy images depicting the combination of DiI (reed) and immune-fluorescence for calbindin-D28k (green) in pyramidal neurons of the CA1 (8-weeks-old mice). Only pyramidal neurons co-labeled with DiI and calbindin-D28k (CB) were used for dendritic spine analysis. (B) Representative sections of 2nd-order apical dendrites from pyramidal CA1 CB-positive neurons in $He^{+/+}$ and $He^{-/-}$ mice. (C) Quantitative analysis from B showing dendritic spine density per micrometer of dendritic length ($t = 4.654$, $p < .001$). (D) Percentage of each morphological type of dendritic spine (see Methods) from $He^{+/+}$ and $He^{-/-}$ mice (genotype x spine type: $F_{(2, 276)} = 4.918$, $p < .01$). (D) Quantification of CB-positive neuronal density in the pyramidal layer of the CA1 in 8-weeks-old $He^{+/+}$ and $He^{-/-}$ mice ($t = 1.199$, $p = .2647$). (F) GluN1 ($t = 4.061$, $p = .0036$), GluN2A, GluN2B ($t = 3.810$, $p = .0052$) and GluN3A protein levels were analyzed in hippocampal samples from 8-week-old $He^{+/+}$ and $He^{-/-}$ mice. Representative immunoblots are shown below the quantification graph for each protein. (G) PSD-95, Chapsyn110, SynGAP and CaMKIIα protein levels were analyzed in hippocampal samples from 8-week-old $He^{+/+}$ and $He^{-/-}$ mice. Representative immunoblots are shown below the quantification graph for each protein. (F) GluN1, GluN2A, GluN2B and GluN3A protein levels were analyzed in hippocampal samples from 8-days-old $He^{+/+}$ and $He^{-/-}$ mice. Representative immunoblots are shown below the quantification graph for each protein. (G) PSD-95, Chapsyn110, SynGAP and CaMKIIα protein levels were analyzed in hippocampal samples from 8-days-old $He^{+/+}$ and $He^{-/-}$ mice. Representative immunoblots are shown below the quantification graph for each protein. Bars represent mean ± SEM. In C and D $He^{+/+}$ ($n = 45$ dendrites) and $He^{-/-}$ ($n = 50$ dendrites) dendrites were used to quantify spine density and density of spine types. In E n = 5 mice/genotype. In F-G n = 5 per genotype. In H–I, $He^{+/+}$ n = 5 and $He^{-/-}$ $n = 6$. **: $p < .01$, ***: $p < .001$ with respect to $He^{+/+}$ mice. Scale bar in A: 70 μm; Scale bar in B: 2 μm. (For interpretation of the references to colour in this figure legend, the reader is referred to the web version of this article.)

density in both, $He^{-/-}$ compared to $He^{+/+}$ mice. We did not find significant changes between genotypes in this parameter (Fig. 5E).

We then sought for putative biochemical changes focusing on synaptic markers due to the alterations observed in LTP (Fig. 4D) and spine density (Fig. 5C-D). Concretely, we evaluated the total protein levels of different *N*-methyl-D-aspartate receptors subunits namely GluN1, GluN2A, GluN2B and Glun3A (Fig. 5F) and postsynaptic density markers namely PSD-95, Chapsyn110, CaMKIIα and SynGAP (Fig. 5G). We found that only GluN1 and GluN2B were significantly decreased in the hippocampus of adult $He^{-/-}$ compared with $He^{+/+}$ mice (Fig. 5F). To gain insight whether these biochemical changes were persistent during the neonatal development or specific for adult ages, we analyzed the levels of all of them at postnatal day 8 (P8) in the hippocampus of $He^{-/-}$ $He^{+/+}$ mice. Surprisingly we did not detect changes either in NMDARs subunits (Fig. 5H) or in postsynaptic density markers (Fig. 5I). Altogether, these results suggest that the impact of the absence of Helios in hippocampal LTP and memory strongly correlates with a modulation of the synapse number and morphology specifically in CB-positive pyramidal cells of the CA1. Furthermore, these changes strongly correlate with a decrease on GluN1 and GluN2B protein levels in adult but not neonatal hippocampi in Helios deficient mice indicating that these changes are not observable until the maturity is reached.

3.6. Identification of VSNL1 as a core gene to mediate hippocampal maturation deficits in Helios deficient mice

Our previous experiments indicate that $He^{-/-}$ mice develop functional, morphological and biochemical alterations dependent on the hippocampal function when they reach adulthood. However, Helios expression is principally limited to developmental stages. Then, we wondered which type of molecular changes during Helios expression could induce such long-term phenotypic outcomes. Then, we first performed a high throughput RNA sequencing in the hippocampus and striatum of $He^{-/-}$ and $He^{+/+}$ embryos (at embryonic day 18), when Helios reaches its peak of expression. The results indicated that 6 hippocampal genes and 4 striatal genes significantly changed in $He^{-/-}$ compared with $He^{+/+}$ E18 embryos including the *Ikzf2* (Helios) gene (Fig. 6A). From these genes, we found particularly interesting the increased expression of the *VSNL1* (Visinin-like 1 protein; VSNL1) gene since it is weakly/non-expressed in the striatum (Braunewell, 2012) and we found its up-regulation only in the hippocampus but not in the striatum of $He^{-/-}$ mice. Additionally, VSNL1 has been largely involved in synaptic plasticity and memory formation (Groblewska et al., 2015). This tissue-specificity could help to explain the divergence that we found between the striatal- and hippocampal-dependent phenotypes in $He^{-/-}$ mice. We then performed a time course only in $He^{+/+}$ samples of VSNL1 expression compared to Helios expression in the developing hippocampus and we found that they followed an opposite pattern. Helios levels were high from embryos stages and then it progressively decreased whereas, in contrast, VSNL1 levels progressively increased to reach the maximum levels at postnatal day 15 (Fig. 6B). Looking at the CA1 neurons in $He^{+/+}$ pups at postnatal day 0 (P0) we found that VSNL1 was highly enriched in Helios-positive neurons of the hippocampal plate (Fig. 6C-D). We also observed that VSNL1 levels were significantly increased in neurons of the hippocampal plate in $He^{-/-}$ compared with $He^{+/+}$ pups at P0 (Fig. 6C and E-F).

Thus, to evaluate whether developmental changes in VSNL1 levels could be relevant for the observed hippocampal-dependent phenotype in $He^{-/-}$ mice we generated several plasmids to express shRNA to inhibit VSNL1 expression (Fig. 7A). From 5 different probes we found that the shRNA4 reduced approximately a 50% of VSNL1 protein expression (Fig. 7A-B) which could be appropriate to prevent the ~35% of VSNL1 increase observed in $He^{-/-}$ pups from Fig. 6. Next, we cultured hippocampal primary neurons from $He^{-/-}$ and $He^{+/+}$ embryos at E18 which were co-transfected at day *in vitro* 21 (DIV21) with a GFP plasmid (to label spines) and the scramble shRNA-mCherry or shRNA4-mCherry to knock-down VSNL1 levels. After 72 h, we analyzed dendritic spine density in selected neurons with pyramidal shape, co-expressing GFP, mCherry and being positive for calbindin (Calbindin 1, 28 kDa; CB-positive pyramidal neurons) (Fig. 7C-D). We found that, as observed in adult mice, $He^{-/-}$ CB-positive pyramidal neurons expressing scramble shRNA showed decreased spine density (Fig. 7E-F). This decrease was significantly restored in $He^{-/-}$ CB-positive pyramidal neurons expressing shRNA4 against VSNL1 (Fig. 7C-D). Altogether, these results indicate that aberrant VSNL1 increased levels in $He^{-/-}$ CB-positive pyramidal neurons are sufficient to induce a loss of its dendritic spine density.

4. Discussion

The heterogeneity of CA1-PNs of the hippocampus is increasingly recognized and theoretical and experimental studies suggest that learning and memory may be produced by the activity of discrete groups of neurons (Buzsaki, 2010; Tonegawa et al., 2015). In addition, it is thought that some of these subpopulations may act as specific cells to control the animal's ability to form spatial memory (Soltesz and Losonczy, 2018). However, the development of molecular, anatomical and functional cues of these cells are still largely undescribed. Here we show that a developmental affection of the transcription factor called Helios in a subpopulation of calbindin positive-CA1-pyramidal neurons (CB-CA1-PNs) is critical for the correct acquisition of spatial memory, CA3-CA1 LTP expression and spine density and morphology.

Lamina-specific neurochemical differences have been described in the CA1-PNs. Different CA1-PNs differ in molecular, structural and physiological characteristics due to their differences in birthdate and specific genetic programs (Soltesz and Losonczy, 2018). We show that Helios is expressed in a specific subpopulation of CB-CA1-PNs. Our results demonstrate that CB-CA1-PNs actively participate in spatial memory. We observe that aberrant development/maturation of Helios-expressing CB-CA1-PNs subpopulation produces dramatic affection of

A

Hippocampus			
Gene	Log2fold	lfcSE	AdjPvale
Ikzf2	232.191	-1.074	3.803e-11
Lancl1	126.247	-0.620	0.000934
Kcne4	31.385	-0.712	0.001031
Pth2r	72.316	1.081	4.806e-10
Wdfy1	1672.722	0.846	2.588e-05
Vsnl1	580.196	0.347	4.585e-05

Striatum			
Gene	Log2fold	lfcSE	AdjPvale
Ikzf2	463.514	-1.145	9.559e-18
Lancl1	162.792	-0.819	2.682e-12
D2hgdh	191.756	-0625	0.0006381
Wdfy1	2758.581	1.032	9.729e-13

B

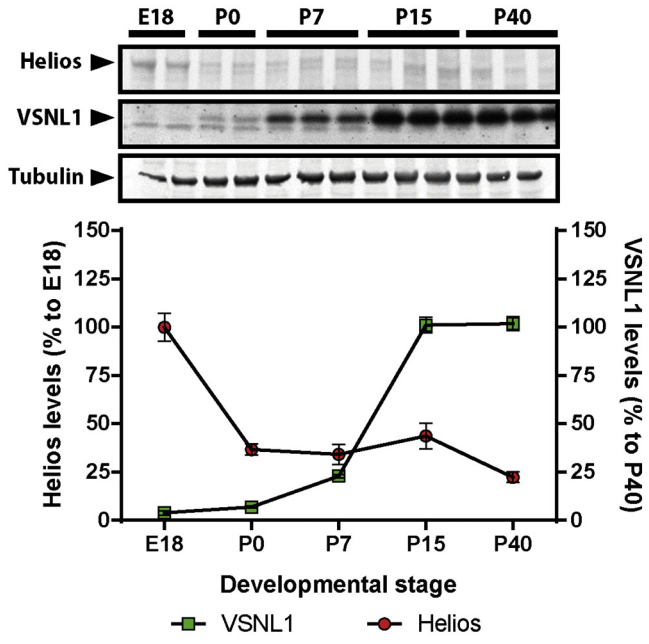

C

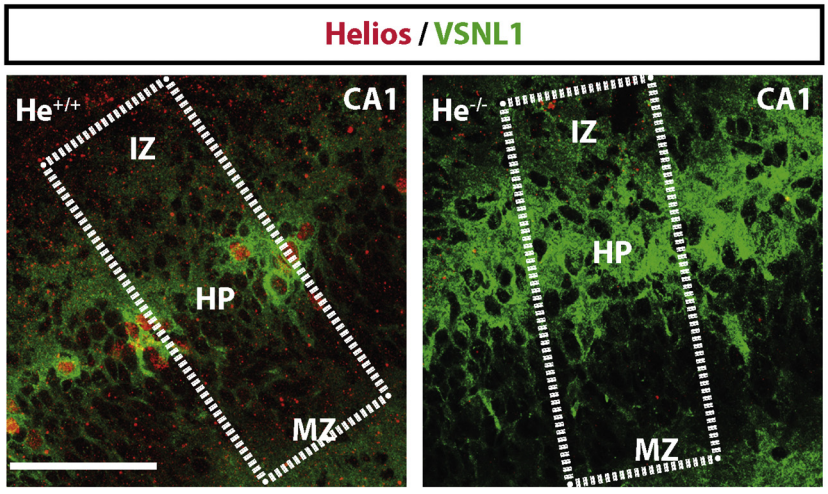

D

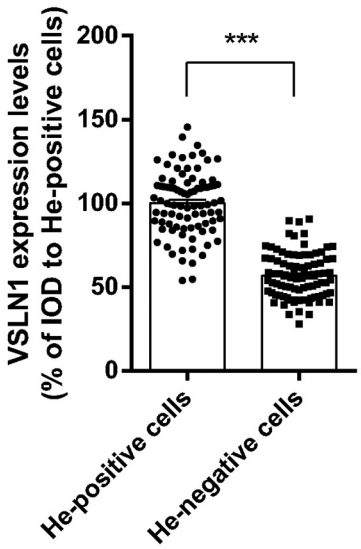

E

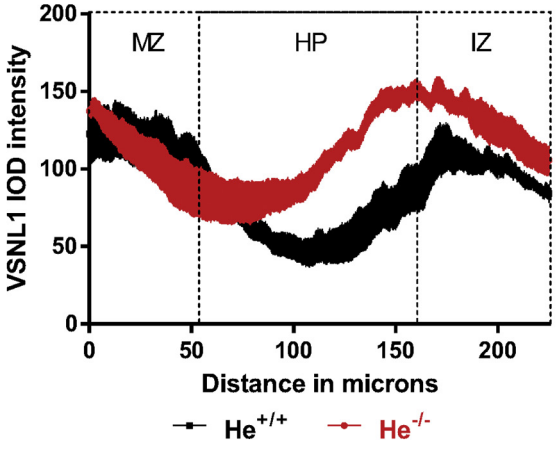

F

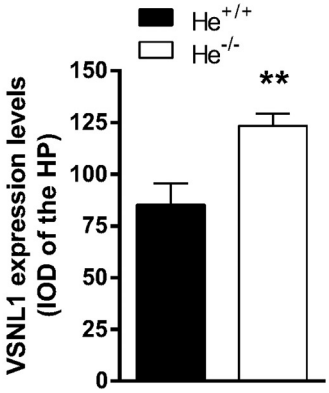

(caption on next page)

Fig. 6. Identification and characterization of VSNL1 in the hippocampus of $He^{+/+}$ and $He^{-/-}$ mice. (A) Embryonic (E18.5) hippocampal and striatal tissue from $He^{+/+}$ and $He^{-/-}$ embryos were subjected to next-generation RNA sequencing. Blue values indicate down-regulated genes and reed values indicate up-regulated genes. 2-fold change and adjusted *p* value are depicted for each gene. (B) Time course of Helios and VSNL1 protein expression only in the $He^{+/+}$ hippocampus. Upper panel shows representative immunoblots at embryonic day 18 and at postnatal days 0, 7, 15 and 40. Lower panel shows the corresponding densitometry quantification. (C) Confocal microscopy images of CA1 immunostained for Helios (red) and VSNL1 (green) in $He^{+/+}$ and $He^{-/-}$ pups at P0. Scale bar: 60 μm. (D) IOD quantification in $He^{+/+}$ pups of VSNL1-positive labeling comparing Helios-positive cells *versus* Helios-negative cells ($t = 17.38$, $p < .001$). (E) IOD quantification of VSNL1-positive labeling from the MZ to the IZ of the CA1 of $He^{+/+}$ and $He^{-/-}$ pups at P0. Using ROIs placed on the top of the dorsal CA1 (as depicted in C by dashed rectangles), we performed a linear intensity profile analysis as a mean IOD. Points in the X axis indicate mean IOD for each row of pixels. (F) Quantification of the HP mean IOD as in E ($t = 3.242$, $p = .0088$). See supplementary methods section for detailed statistics of the next-generation RNA sequencing in A. Bars represent mean ± SEM. In B n = 6 mice/group; in D $n = 88$ cells from 5 mice/genotype were evaluated; In E and F n = 6 mice/genotype. All data was analyzed using two-tailed Student's t-test. **: $p < .01$, ***: $p < .001$ with respect to $He^{+/+}$ mice. IZ: Intermediate zone, dHP: Dorsal hippocampal plate, sHP: Superficial hippocampal plate. (For interpretation of the references to colour in this figure legend, the reader is referred to the web version of this article.)

CA3-CA1 LTP. Accordingly, CA3 Schaffer collateral excitation is stronger in CB-CA1-PNs (Valero et al., 2015) and spatial learning performances strongly correlate with CA3-CA1 LTP induction (Morris and Frey, 1997; Shapiro, 2001), suggesting a direct correlation between affectation of LTP in Helios CB-CA1-PNs and spatial memory.

We also found that Helios genetic deletion does not affect the general dendritic arborization, but it induced dendritic spine number loss specifically in CB-CA1-PNs. Supporting our results, it has been shown that spatial memory and associative learning have been strongly associated with changes on hippocampal dendritic spines (Leuner et al., 2003; Moser et al., 1994). Furthermore, specific dendritic spine loss in CB-CA1-PNs could account for their essential role in the expression and maintenance of hippocampal LTP and spatial learning (Jouvenceau et al., 1999; Molinari et al., 1996). Similarly, the FMR1 KO mice, a model of Fragile X syndrome (FXS), showed deficits in spatial learning which were accompanied of altered functions in CB-CA1-PNs (Real et al., 2011). On the other hand, present findings also demonstrate that the main synaptic morphological alteration was found in “thin-like” spines whose are considered the learning spines due to their prominent motility (Bourne and Harris, 2007). Strengthening our data, it has been shown that decreased density of thin spines is associated with impairments in several cognitive tasks (Dumitriu et al., 2010) and treatments aimed to counteract cognitive decline in neurological disorders result in an increase in numbers of thin spines (Bourne and Harris, 2007).

Strikingly, we observed that early postnatal neurological functions were almost unaffected in $He^{-/-}$ mice whereas at young/adult stages, $He^{-/-}$ mice displayed moderate and specific spatial learning and memory impairments. These results are apparently opposed to the finding that hippocampal Helios expression peaks around peri-natal stages, when CA1 neurons have finished their positioning and begin to mature (Altman and Bayer, 1990a; Altman and Bayer, 1990c; Altman and Bayer, 1990b; Bayer, 1980a; Bayer, 1980b; Danglot et al., 2006). However, we hypothesize that developmental deficiencies in Helios expressing CB-CA1-PNs induce long-term outcome effects that are only observed when these hippocampal synapses are completely functional at adult stages (Baudry et al., 1981; Dudek and Bear, 1993; Harris and Teyler, 1984) but not at early postnatal stages (Durand and Konnerth, 1996). In this line, CA1 synapses at first postnatal days are prominently silent and it is hard to induce LTP on them during the first postnatal week, whereas robust LTP can be induced after the second week (Baudry et al., 1981; Harris and Teyler, 1984). Synaptogenesis occurs in the CA1 from P2 onwards (Amaral and Dent, 1981; Buchs et al., 1993), and spines become more stable and more mature between P15 and P35 (Fiala et al., 1998; Harris et al., 1992). Supporting our hypothesis, the dysregulation of other specific developmental expressed genes (Bhatt et al., 2009; van et al., 2013) or treatments with drugs during early life stages have been shown to induce long-term outcome effects in neural function and synaptic plasticity (Kataoka et al., 2013; Takuma et al., 2014; Xiao et al., 2016).

The mechanism that instruct the assembly of fine-scale features of synaptic connectivity in CB-CA1-PNs are only beginning to be understood. Growing evidences indicate that spines formation and synaptic connectivity occur in the absence of glutamate release (Lu et al., 2013; Varoqueaux et al., 2002; Verhage et al., 2000). In contrast, several authors claim that initial development of dendrites, synapses and spines are mostly controlled by cell-intrinsic genetic programs (Lu et al., 2013). At the present time no specific intrinsic genetic program has been associated with spinogenic processes in CB-CA1-PNs. Here we show that a specific transcription factor, Helios, is critical for the correct production of thin-like dendritic spines, suggesting an extremely fine molecular regulation of the spinogenesis in the CB-CA1-PNs subpopulation. In this line, a putative cell intrinsic genetic program mediating such phenomena could involve the regulation of intracellular calcium homeostasis. We identified VSNL1, a neuronal calcium sensor protein, as the principal Helios downstream candidate that could explain our divergent striatal- and hippocampal-dependent phenotypes since VSNL1 was observed to be increased only in the hippocampi from $He^{-/-}$ mice compared to $He^{+/+}$ mice. Indeed, VSNL1 expression is almost absent in control striatal tissue (Paterlini et al., 2000). Within the hippocampus, VSNL1 is expressed in pyramidal neurons of the CA1 and in calretinin-positive interneurons (Bernstein et al., 2002). In contrast to Helios, VSNL1 expression increases progressively during hippocampal development (present results) and it reaches its maximum levels in adulthood (Gierke et al., 2004). We hypothesize that Helios could modulate spinogenesis through a tight regulation of VSNL1 expression. Reinforcing this idea, it has been proposed that during the maturation of neural circuits, the most prominent group of up-regulated genes consists on calcium-dependent membrane-binding proteins, including VSNL1 (Yamatani et al., 2010). Although a direct Helios regulation of VSNL1 cannot be ruled out, Helios could also control VSNL1 expression indirectly. Supporting the latter idea, it is known that Helios plays a role as a co-factor together with other transcription factors such as Nuclear Respiratory Factor-1 (NRF1) as demonstrated in previous analysis of DNA regions in which Helios showed significant enrichment of NRF1 binding motifs (Kim et al., 2015). NRF1 is a good candidate to link Helios with VSNL1 since it is able to regulate VSNL1 gene transcription (Fu et al., 2009) and in turn, NRF1 is associated with Alzheimer's disease (Preciados et al., 2016) in correlation with the spatial learning deficits observed in mice devoid of Helios. We hypothesize then that a lack of the Helios repressive function on gene expression in $He^{-/-}$ mice would induce a premature increase on VSNL1 expression in CB-CA1-PNs which in turn would negatively influence the spine formation and maintenance. Similarly, overexpression of VSNL1 as well as other calcium sensors are capable to reduce axon outgrowth and branching in other neural systems (Angaut-Petit et al., 1998; Hui et al., 2007; Yamatani et al., 2010). VSNL1 overexpression might influence certain neuronal processes such as structural synaptic plasticity and neuronal maturation *via* regulation of cAMP and cGMP production (Lin et al., 2002), (Braunewell et al., 2011a, 2011b). Accordingly, a sustained and occluded expression of the cAMP-PKA pathways can induce deficits in hippocampal-related learning and memory (Carlyle et al., 2014; Giralt et al., 2011b; Ramos et al., 2003), possibly, *via* modulating neuronal morphology during development (Cai et al., 2001).

In summary, proper CB-CA1-PNs spine maturation depends on a homeostatic expression of VSNL1. VSNL1 levels during development are tightly controlled by Helios transcription regulation in this neuronal

A

Construct	5′-3′ sequence	% inhibition
shRNA 1	CGCGTGAGTTCAATGAGCATGAGCTTCAAGAGAGCTCATGCTCATTGAACTCTTTTTTCTCGAGAT CGATCTCGAGAAAAAAAGAGTTCAATGAGCATGAGCTCTCTTGAAGCTCATGCTCATTGAACTCA	Not detected
shRNA 2	CGCGTGTTCCAGCAGCTCTATGTGTTCAAGAGACACATAGAGCTGCTGGAACTTTTTTCTCGAGAT CGATCTCGAGAAAAAAAGTTCCAGCAGCTCTATGTGTCTCTTGAACACATAGAGCTGCTGGAACA	15% reduction
shRNA 3	CGCGTGGGCTTTCAACATGTATGATTCAAGAGATCATACATGTTGAAAGCCCTTTTTTCTCGAGAT CGATCTCGAGAAAAAAAGGGCTTTCAACATGTATGATCTCTTGAATCATACATGTTGAAAGCCCA	No effect
shRNA 4	CGCGTGCTGGAGATTATCGAGGCTTTCAAGAGAAGCCTCGATAATCTCCAGCTTTTTTCTCGAGAT CGATCTCGAGAAAAAAAGCTGGAGATTATCGAGGCTTCTCTTGAAAGCCTCGATAATCTCCAGCA	50% reduction
shRNA 5	CGCGTGCCTTAATTCTTACCTCATTTTTCAAGAGAAAATGAGGTAAGAATTAAGGCTTTTTTCTCGAGAT	Not detected

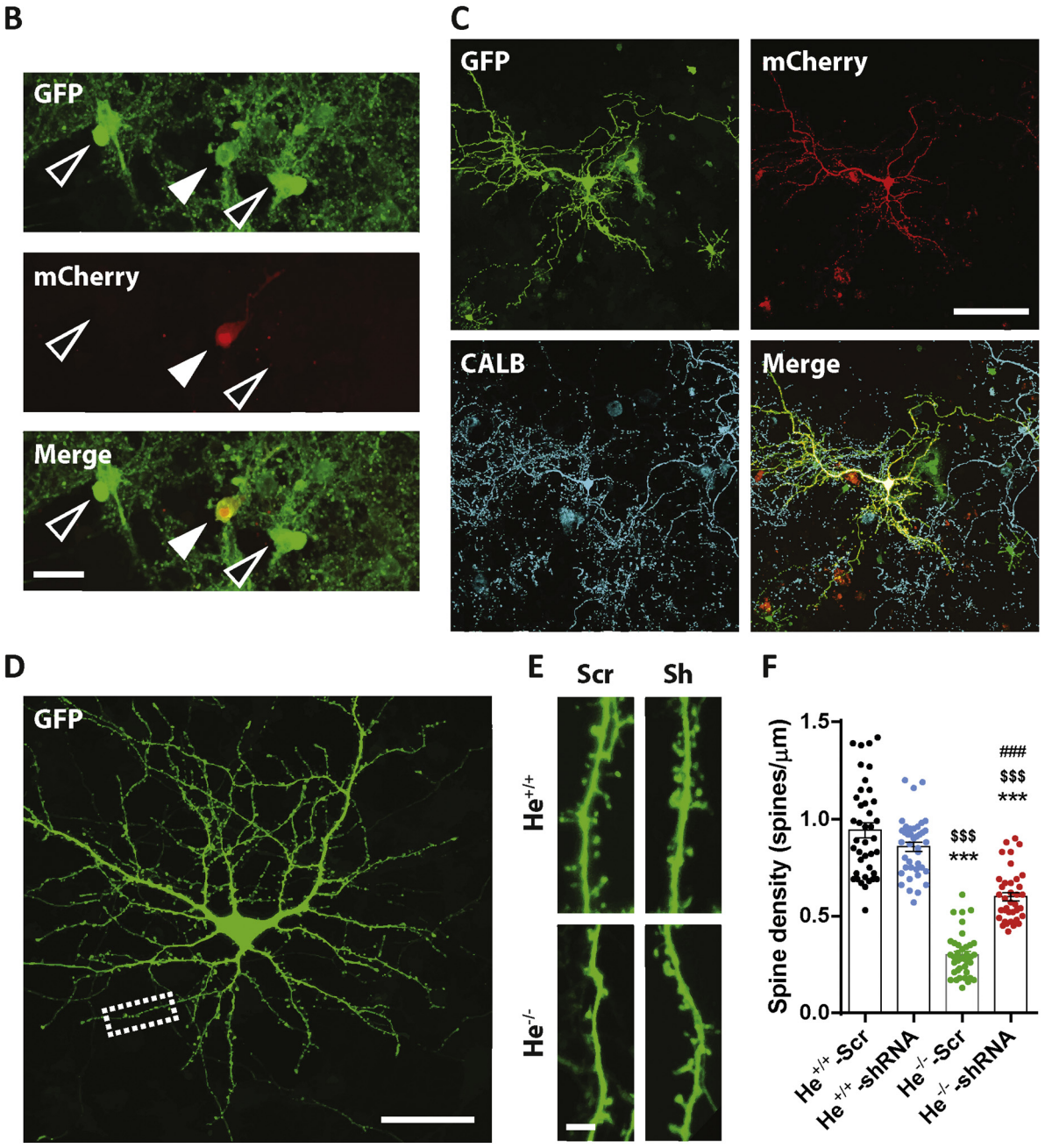

(caption on next page)

Fig. 7. Effects of VSNL1 levels normalization in $He^{+/+}$ and $He^{-/-}$ CA1 CB-Positive Neurons. (A) Pyramidal neurons at day *in vitro* 21 were transfected with 5 different plasmids expressing shRNA constructs designed to prevent VSNL1 expression. (A and B) Note the significant reduction of VSNL1 expression provoked by the plasmid expressing the shRNA 4. The plasmid expressing the shRNA 4 was chosen for subsequent studies from B to F. Scale bar: 30 μm. (C) Pyramidal neurons at day *in vitro* 21 were co-transfected with a plasmid expressing GFP (green) and the plasmid expressing the shRNA 4 (reed/mCherry). 72 h after transfection cells were fixed and labeled for calbindin-D28k (CB). Scale bar: 50 μm. (C-D) Only cells with pyramidal-like shapes and co-labeled with GFP/mCherry/CB were used for the dendritic spine density analysis. Scale bar: 25 μm. (E) Representative dendrite sections labeled with GFP and used for dendritic spines density analysis. Scale bar: 3 μm. (F) Spine density quantification (Group effect: $F_{(3,156)} = 9.846$, $p < .001$) of results as in E ($n = 40$ dendrites/group from 3 different cultures). Bars represent mean ± SEM. For statistical analysis one-way ANOVA with the Tukey's *post hoc* test was used. ***: $p < .001$ with respect to $He^{+/+}$-Scr group; $^{\$\$\$}$: $p < .001$ with respect to $He^{+/+}$-shRNA group; $^{\#\#\#}$: $p < .001$ with respect to $He^{-/-}$-Scr group. Scr: Scramble; shRNA: shRNA 4. (For interpretation of the references to colour in this figure legend, the reader is referred to the web version of this article.)

subpopulation. An incorrect balance of this complex hippocampal system during development would induce a long-lasting and specific incapacity to form spatial memory traces during adulthood as observed in several neuropsychiatric and cognitive disorders.

Ethics approval

Mouse experiments were approved by local committees [Universitat de Barcelona, CEEA (133/10) and Generalitat de Catalunya (DAAM 5712)].

Funding

This study was supported by grants from the Ministerio de Economia y Competitividad (SAF 2014-57160-R to JA; BFU2017-88393-P, to EDM; SAF2016-76340R to ES; and SAF2015-66505-R to J.M.C;), Spain; Instituto de Salud Carlos III, Ministerio de Economia y Competitividad and European Regional Development Fund (ERDF) [CIBERNED, to JA and ES; *Fondo de Investigaciones Sanitarias* (PI11/00704) to MP; and RETICS (RD16/0011/0011 to JCS; RD16/0011/0012 to JMC, Red de Terapia Celular), to JMC], Spain; Generalitat de Catalunya (2017SGR-1095 to JA, and 2017SGR-1408 to JMC), Spain; and ADVANCE(CAT) with the support of ACCIÓ (Catalonia Trade & Investment; Generalitat de Catalunya), the European Community under the Catalonian ERDF operational program 2014–2020], Spain and from Ministerio de Ciencia, Innovación y Universidades (RTI2018-094678-A-I00 to AG; RTI2018-099001-B-I00 to JMC). AG is a Ramón y Cajal fellow (RYC-2016-19466).

Authors' contributions

A.G. conceived and carried out most experiments, analyzed and interpreted results and wrote the manuscript. V.B. carried out experiments related to gene gun and primary cultures. M.P. and R.-M.I. carried out the experiments in embryonic samples. S.R. carried out the Golgi Cox staining and some perinatal ICC experiments at embryonic stages and C.B. performed the electronic microscopy. L.M.-P. helped with the RNAseq experiments. A.Z.-M. And J.B. performed the electrophysiology experiments. E.B. and M.P. carried out the necropsy experiments and tissue characterization of mutant mice. A.G.-T. And J.S. generated the VSNL1 plasmids. J.A. supervised the histological experiments. S.G. supervised the biochemical experiments. M.P. supervised the golgi experiments. E.S. supervised the electronic microscopy experiments. E.D.M. supervised the electrophysiological experiments. J.M.C. conceived and supervised the study, analyzed results and wrote the manuscript.

Declaration of Competing Interest

The authors have no competing financial interest to declare.

Acknowledgements

We are very grateful to Jean-Antoine Girault, Institut du Fer à Moulin (Paris, France) for his comments and advise. We thank Ana López, Maria Teresa Muñoz for technical assistance. We also thank Dr. Isabel Pérez Otaño (Centro de Investigaciones Médicas Aplicadas, Pamplona. Spain) for her generous gift of the anti-GluN3A antibody. The Rat-401 monoclonal anti-nestin antibody developed by S. Hockfield was obtained from the Development Studies Hybridoma Bank developed under the auspices of the NICHD and maintained by the Department of Biological Science, University of Iowa, Iowa City, Iowa.

Appendix A. Supplementary data

Supplementary data to this article can be found online at https://doi.org/10.1016/j.expneurol.2019.113095.

References

Agoston, D.V., Szemes, M., Dobi, A., Palkovits, M., Georgopoulos, K., Gyorgy, A., Ring, M.A., 2007. Ikaros is expressed in developing striatal neurons and involved in enkephalinergic differentiation. J. Neurochem. 102, 1805–1816.
Altman, J., Bayer, S.A., 1990a. Migration and distribution of two populations of hippocampal granule cell precursors during the perinatal and postnatal periods. J. Comp. Neurol. 301, 365–381.
Altman, J., Bayer, S.A., 1990b. Mosaic organization of the hippocampal neuroepithelium and the multiple germinal sources of dentate granule cells. J. Comp. Neurol. 301, 325–342.
Altman, J., Bayer, S.A., 1990c. Prolonged sojourn of developing pyramidal cells in the intermediate zone of the hippocampus and their settling in the stratum pyramidale. J. Comp. Neurol. 301, 343–364.
Amaral, D.G., Dent, J.A., 1981. Development of the mossy fibers of the dentate gyrus: I. A light and electron microscopic study of the mossy fibers and their expansions. J. Comp. Neurol. 195, 51–86.
Angaut-Petit, D., Toth, P., Rogero, O., Faille, L., Tejedor, F.J., Ferrus, A., 1998. Enhanced neurotransmitter release is associated with reduction of neuronal branching in a Drosophila mutant overexpressing frequenin. Eur. J. Neurosci. 10, 423–434.
Baudry, M., Arst, D., Oliver, M., Lynch, G., 1981. Development of glutamate binding sites and their regulation by calcium in rat hippocampus. Brain Res. 227, 37–48.
Bayer, S.A., 1980a. Development of the hippocampal region in the rat. I. Neurogenesis examined with 3H-thymidine autoradiography. J. Comp. Neurol. 190, 87–114.
Bayer, S.A., 1980b. Development of the hippocampal region in the rat. II. Morphogenesis during embryonic and early postnatal life. J. Comp. Neurol. 190, 115–134.
Bernstein, H.G., Braunewell, K.H., Spilker, C., Danos, P., Baumann, B., Funke, S., Diekmann, S., Gundelfinger, E.D., Bogerts, B., 2002. Hippocampal expression of the calcium sensor protein visinin-like protein-1 in schizophrenia. Neuroreport 13, 393–396.
Bhatt, D.H., Zhang, S., Gan, W.B., 2009. Dendritic spine dynamics. Annu. Rev. Physiol. 71, 261–282.
Bourin, M., Hascoet, M., 2003. The mouse light/dark box test. Eur. J. Pharmacol. 463, 55–65.
Bourne, J., Harris, K.M., 2007. Do thin spines learn to be mushroom spines that remember? Curr. Opin. Neurobiol. 17, 381–386.
Bourne, J.N., Harris, K.M., 2011. Coordination of size and number of excitatory and inhibitory synapses results in a balanced structural plasticity along mature hippocampal CA1 dendrites during LTP. Hippocampus. 21 (4), 354–373.
Braunewell, K.H., 2012. The visinin-like proteins VILIP-1 and VILIP-3 in Alzheimer's disease-old wine in new bottles. Front. Mol. Neurosci. 5, 20.
Braunewell, K.H., Dwary, A.D., Richter, F., Trappe, K., Zhao, C., Giegling, I., Schönrath, K., Rujescu, D., 2011a. Association of VSNL1 with schizophrenia, frontal cortical function, and biological significance for its gene product as a modulator of cAMP levels and neuronal morphology. Transl. Psychiatry 1, e22.
Braunewell, K.H., Dwary, A.D., Richter, F., Trappe, K., Zhao, C., Giegling, I., Schonrath, K., Rujescu, D., 2011b. Association of VSNL1 with schizophrenia, frontal cortical function, and biological significance for its gene product as a modulator of cAMP levels and neuronal morphology. Transl. Psychiatry 1, e22.
Brito, V., Giralt, A., Enriquez-Barreto, L., Puigdellivol, M., Suelves, N., Zamora-Moratalla, A., Ballesteros, J.J., Martin, E.D., Dominguez-Iturza, N., Morales, M., Alberch, J., Gines, S., 2014. Neurotrophin receptor p75(NTR) mediates Huntington's disease-associated synaptic and memory dysfunction. J. Clin. Invest. 124, 4411–4428.
Brown, S.P., Hestrin, S., 2009. Cell-type identity: a key to unlocking the function of

neocortical circuits. Curr. Opin. Neurobiol. 19, 415–421.
Buchs, P.A., Stoppini, L., Muller, D., 1993. Structural modifications associated with synaptic development in area CA1 of rat hippocampal organotypic cultures. Brain Res. Dev. Brain Res. 71, 81–91.
Buzsaki, G., 2010. Neural syntax: cell assemblies, synapsembles, and readers. Neuron 68, 362–385.
Cai, D., Qiu, J., Cao, Z., McAtee, M., Bregman, B.S., Filbin, M.T., 2001. Neuronal cyclic AMP controls the developmental loss in ability of axons to regenerate. J. Neurosci. 21, 4731–4739.
Cai, Q., Dierich, A., Oulad-Abdelghani, M., Chan, S., Kastner, P., 2009. Helios deficiency has minimal impact on T cell development and function. J. Immunol. 183, 2303–2311.
Carlyle, B.C., Nairn, A.C., Wang, M., Yang, Y., Jin, L.E., Simen, A.A., Ramos, B.P., Bordner, K.A., Craft, G.E., Davies, P., Pletikos, M., Sestan, N., Arnsten, A.F., Paspalas, C.D., 2014. cAMP-PKA phosphorylation of tau confers risk for degeneration in aging association cortex. Proc. Natl. Acad. Sci. U. S. A. 111, 5036–5041.
Cembrowski, M.S., Bachman, J.L., Wang, L., Sugino, K., Shields, B.C., Spruston, N., 2016. Spatial gene-expression gradients underlie prominent heterogeneity of CA1 pyramidal neurons. Neuron 89, 351–368.
Cobb, B.S., Smale, S.T., 2005. Ikaros-family proteins: in search of molecular functions during lymphocyte development. Curr. Top. Microbiol. Immunol. 290, 29–47.
Danglot, L., Triller, A., Marty, S., 2006. The development of hippocampal interneurons in rodents. Hippocampus 16, 1032–1060.
Deguchi, Y., Donato, F., Galimberti, I., Cabuy, E., Caroni, P., 2011. Temporally matched subpopulations of selectively interconnected principal neurons in the hippocampus. Nat. Neurosci. 14, 495–504.
Dierssen, M., Fotaki, V., Martinez de, L.M., Gratacos, M., Arbones, M., Fillat, C., Estivill, X., 2002. Neurobehavioral development of two mouse lines commonly used in transgenic studies. Pharmacol. Biochem. Behav. 73, 19–25.
Dimsdale-Zucker, H.R., Ritchey, M., Ekstrom, A.D., Yonelinas, A.P., Ranganath, C., 2018. CA1 and CA3 differentially support spontaneous retrieval of episodic contexts within human hippocampal subfields. Nat. Commun. 9 (1), 294 18.
Dong, H.W., Swanson, L.W., Chen, L., Fanselow, M.S., Toga, A.W., 2009. Genomic-anatomic evidence for distinct functional domains in hippocampal field CA1. Proc. Natl. Acad. Sci. U. S. A. 106, 11794–11799.
Dudek, S.M., Bear, M.F., 1993. Bidirectional long-term modification of synaptic effectiveness in the adult and immature hippocampus. J. Neurosci. 13, 2910–2918.
Dumitriu, D., Hao, J., Hara, Y., Kaufmann, J., Janssen, W.G., Lou, W., Rapp, P.R., Morrison, J.H., 2010. Selective changes in thin spine density and morphology in monkey prefrontal cortex correlate with aging-related cognitive impairment. J. Neurosci. 30, 7507–7515.
Durand, G.M., Konnerth, A., 1996. Long-term potentiation as a mechanism of functional synapse induction in the developing hippocampus. J. Physiol. Paris 90, 313–315.
Fiala, J.C., Feinberg, M., Popov, V., Harris, K.M., 1998. Synaptogenesis via dendritic filopodia in developing hippocampal area CA1. J. Neurosci. 18, 8900–8911.
Fiala, J.C., Spacek, J., Harris, K.M., 2002. Dendritic spine pathology: cause or consequence of neurological disorders? Brain Res. Brain Res. Rev. 39, 29–54.
Fox, W.M., 1965. Reflex-ontogeny and behavioural development of the mouse. Anim. Behav. 13, 234–241.
Fu, J., Zhang, J., Jin, F., Patchefsky, J., Braunewell, K.H., Klein-Szanto, A.J., 2009. Promoter regulation of the visinin-like subfamily of neuronal calcium sensor proteins by nuclear respiratory factor-1. J. Biol. Chem. 284, 27577–27586.
Gierke, P., Zhao, C., Brackmann, M., Linke, B., Heinemann, U., Braunewell, K.H., 2004. Expression analysis of members of the neuronal calcium sensor protein family: combining bioinformatics and Western blot analysis. Biochem. Biophys. Res. Commun. 323, 38–43.
Giralt, A., Friedman, H.C., Caneda-Ferron, B., Urban, N., Moreno, E., Rubio, N., Blanco, J., Peterson, A., Canals, J.M., Alberch, J., 2010. BDNF regulation under GFAP promoter provides engineered astrocytes as a new approach for long-term protection in Huntington's disease. Gene Ther. 17, 1294–1308.
Giralt, A., Carreton, O., Lao-Peregrin, C., Martin, E.D., Alberch, J., 2011a. Conditional BDNF release under pathological conditions improves Huntington's disease pathology by delaying neuronal dysfunction. Mol. Neurodegener. 6, 71.
Giralt, A., Saavedra, A., Carreton, O., Xifro, X., Alberch, J., Perez-Navarro, E., 2011b. Increased PKA signaling disrupts recognition memory and spatial memory: role in Huntington's disease. Hum. Mol. Genet. 20, 4232–4247.
Giralt, A., Sanchis, D., Cherubini, M., Ginés, S., Cañas, X., Comella, J.X., Alberch, J., 2013. Neurobehavioral characterization of endonuclease G knockout mice reveals a new putative molecular player in the regulation of anxiety. Exp. Neurol. 247, 122–129.
Giralt, A., Brito, V., Chevy, Q., Simonnet, C., Otsu, Y., Cifuentes-Diaz, C., de, P.B., Coura, R., Alberch, J., Gines, S., Poncer, J.C., Girault, J.A., 2017. Pyk2 modulates hippocampal excitatory synapses and contributes to cognitive deficits in a Huntington's disease model. Nat. Commun. 8, 15592.
Groblewska, M., Muszynski, P., Wojtulewska-Supron, A., Kulczynska-Przybik, A., Mroczko, B., 2015. The role of Visinin-like Protein-1 in the pathophysiology of Alzheimer's disease. J. Alzheimers Dis. 47, 17–32.
Harris, K.M., Teyler, T.J., 1984. Developmental onset of long-term potentiation in area CA1 of the rat hippocampus. J. Physiol. 346, 27–48.
Harris, K.M., Jensen, F.E., Tsao, B., 1992. Three-dimensional structure of dendritic spines and synapses in rat hippocampus (CA1) at postnatal day 15 and adult ages: implications for the maturation of synaptic physiology and long-term potentiation. J. Neurosci. 12, 2685–2705.
Hollingworth, P., Sweet, R., Sims, R., Harold, D., Russo, G., Abraham, R., Stretton, A., Jones, N., Gerrish, A., Chapman, J., Ivanov, D., Moskvina, V., Lovestone, S., Priotsi, P., Lupton, M., Brayne, C., Gill, M., Lawlor, B., Lynch, A., Craig, D., McGuinness, B., Johnston, J., Holmes, C., Livingston, G., Bass, N.J., Gurling, H., McQuillin, A., Consortium, G.E.R.A.D., National Institute on Aging Late-Onset Alzheimer's Disease Family Study Group, Holmans, P., Jones, L., Devlin, B., Klei, L., Barmada, M.M., Demirci, F.Y., De Kosky, S.T., Lopez, O.L., Passmore, P., Owen, M.J., O'Donovan, M.C., Mayeux, R., Kamboh, M.I., Williams, J., 2012. Genome-wide association study of Alzheimer's disease with psychotic symptoms. Mol. Psychiatry 1316–1327 (12).
Huang, C., Chen, M., Pang, D., Bi, D., Zou, Y., Xia, X., Yang, W., Luo, L., Deng, R., Tan, H., Zhou, L., Yu, S., Guo, L., Du, X., Cui, Y., Hu, J., Mao, Q., Worley, P.F., Xiao, B., 2014. Developmental and activity-dependent expression of LanCL1 confers antioxidant activity required for neuronal survival. Dev. Cell 30, 479–487.
Hui, K., Fei, G.H., Saab, B.J., Su, J., Roder, J.C., Feng, Z.P., 2007. Neuronal calcium sensor-1 modulation of optimal calcium level for neurite outgrowth. Development 134, 4479–4489.
Jammalamadaka, A., Banerjee, S., Manjunath, B.S., Kosik, K.S., 2013. Statistical analysis of dendritic spine distributions in rat hippocampal cultures. BMC. Bioinforma. 14, 287.
Jouvenceau, A., Potier, B., Battini, R., Ferrari, S., Dutar, P., Billard, J.M., 1999. Glutamatergic synaptic responses and long-term potentiation are impaired in the CA1 hippocampal area of calbindin D(28k)-deficient mice. Synapse 33, 172–180.
Kataoka, S., Takuma, K., Hara, Y., Maeda, Y., Ago, Y., Matsuda, T., 2013. Autism-like behaviours with transient histone hyperacetylation in mice treated prenatally with valproic acid. Int. J. Neuropsychopharmacol. 16, 91–103.
Kim, H.J., Barnitz, R.A., Kreslavsky, T., Brown, F.D., Moffett, H., Lemieux, M.E., Kaygusuz, Y., Meissner, T., Holderried, T.A., Chan, S., Kastner, P., Haining, W.N., Cantor, H., 2015. Stable inhibitory activity of regulatory T cells requires the transcription factor Helios. Science 350, 334–339.
Leuner, B., Falduto, J., Shors, T.J., 2003. Associative memory formation increases the observation of dendritic spines in the hippocampus. J. Neurosci. 23, 659–665.
Lex, B., Sommer, S., Hauber, W., 2011. The role of dopamine in the dorsomedial striatum in place and response learning. Neuroscience 172, 212–218.
Li, J.T., Zhao, Y.Y., Wang, H.L., Wang, X.D., Su, Y.A., Si, T.M., 2015. Long-term effects of neonatal exposure to MK-801 on recognition memory and excitatory-inhibitory balance in rat hippocampus. Neuroscience 308, 134–143.
Lin, L., Braunewell, K.H., Gundelfinger, E.D., Anand, R., 2002. Functional analysis of calcium-binding EF-hand motifs of visinin-like protein-1. Biochem. Biophys. Res. Commun. 296, 827–832.
Lu, W., Bushong, E.A., Shih, T.P., Ellisman, M.H., Nicoll, R.A., 2013. The cell-autonomous role of excitatory synaptic transmission in the regulation of neuronal structure and function. Neuron 78, 433–439.
Martin-Ibanez, R., Crespo, E., Urban, N., Sergent-Tanguy, S., Herranz, C., Jaumot, M., Valiente, M., Long, J.E., Pineda, J.R., Andreu, C., Rubenstein, J.L., Marin, O., Georgopoulos, K., Mengod, G., Farinas, I., Bachs, O., Alberch, J., Canals, J.M., 2010. Ikaros-1 couples cell cycle arrest of late striatal precursors with neurogenesis of enkephalinergic neurons. J. Comp. Neurol. 518, 329–351.
Martin-Ibanez, R., Crespo, E., Esgleas, M., Urban, N., Wang, B., Waclaw, R., Georgopoulos, K., Martinez, S., Campbell, K., Vicario-Abejon, C., Alberch, J., Chan, S., Kastner, P., Rubenstein, J.L., Canals, J.M., 2012. Helios transcription factor expression depends on Gsx2 and Dlx1&2 function in developing striatal matrix neurons. Stem Cells Dev. 21, 2239–2251.
Metz, G.A., Schwab, M.E., 2004. Behavioral characterization in a comprehensive mouse test battery reveals motor and sensory impairments in growth-associated protein-43 null mutant mice. Neuroscience 129, 563–574.
Molinari, S., Battini, R., Ferrari, S., Pozzi, L., Killcross, A.S., Robbins, T.W., Jouvenceau, A., Billard, J.M., Dutar, P., Lamour, Y., Baker, W.A., Cox, H., Emson, P.C., 1996. Deficits in memory and hippocampal long-term potentiation in mice with reduced calbindin D28K expression. Proc. Natl. Acad. Sci. U. S. A. 93, 8028–8033.
Morris, R.G., Frey, U., 1997. Hippocampal synaptic plasticity: role in spatial learning or the automatic recording of attended experience? Philos. Trans. R. Soc. Lond. Ser. B Biol. Sci. 352, 1489–1503.
Moser, M.B., Trommald, M., Andersen, P., 1994. An increase in dendritic spine density on hippocampal CA1 pyramidal cells following spatial learning in adult rats suggests the formation of new synapses. Proc. Natl. Acad. Sci. U. S. A. 91, 12673–12675.
Packard, M.G., Knowlton, B.J., 2002. Learning and memory functions of the basal ganglia. Annu. Rev. Neurosci. 25, 563–593.
Paterlini, M., Revilla, V., Grant, A.L., Wisden, W., 2000. Expression of the neuronal calcium sensor protein family in the rat brain. Neuroscience 99, 205–216.
Preciados, M., Yoo, C., Roy, D., 2016. Estrogenic endocrine disrupting chemicals influencing NRF1 regulated gene networks in the development of complex human brain diseases. Int. J. Mol. Sci. 17.
Ramos, B.P., Birnbaum, S.G., Lindenmayer, I., Newton, S.S., Duman, R.S., Arnsten, A.F., 2003. Dysregulation of protein kinase a signaling in the aged prefrontal cortex: new strategy for treating age-related cognitive decline. Neuron 40, 835–845.
Real, M.A., Simon, M.P., Heredia, R., de, D.Y., Guirado, S., 2011. Phenotypic changes in calbindin D28K immunoreactivity in the hippocampus of Fmr1 knockout mice. J. Comp. Neurol. 519, 2622–2636.
Sellami, A., Al Abed, A.S., Brayda-Bruno, L., Etchamendy, N., Valério, S., Oulé, M., Pantaléon, L., Lamothe, V., Potier, M., Bernard, K., Jabourian, M., Herry, C., Mons, N., Piazza, P.V., Eichenbaum, H., Marighetto, A., 2017. Temporal binding function of dorsal CA1 is critical for declarative memory formation. Proc. Natl. Acad. Sci. U. S. A. 114 (38), 10262–10267.
Shapiro, M., 2001. Plasticity, hippocampal place cells, and cognitive maps. Arch. Neurol. 58, 874–881.
Slomianka, L., Amrein, I., Knuesel, I., Sorensen, J.C., Wolfer, D.P., 2011. Hippocampal pyramidal cells: the reemergence of cortical lamination. Brain Struct. Funct. 216, 301–317.
Soltesz, I., Losonczy, A., 2018. CA1 pyramidal cell diversity enabling parallel information processing in the hippocampus. Nat. Neurosci. 21, 484–493.

Stevenson, R.F., Zheng, J., Mnatsakanyan, L., Vadera, S., Knight, R.T., Lin, J.J., Yassa, M.A., 2018. Hippocampal CA1 gamma power predicts the precision of spatial memory judgments. Proc. Natl. Acad. Sci. U. S. A. 115 (40), 10148–10153.

Takuma, K., Hara, Y., Kataoka, S., Kawanai, T., Maeda, Y., Watanabe, R., Takano, E., Hayata-Takano, A., Hashimoto, H., Ago, Y., Matsuda, T., 2014. Chronic treatment with valproic acid or sodium butyrate attenuates novel object recognition deficits and hippocampal dendritic spine loss in a mouse model of autism. Pharmacol. Biochem. Behav. 126, 43–49.

Thompson, C.L., Pathak, S.D., Jeromin, A., Ng, L.L., MacPherson, C.R., Mortrud, M.T., Cusick, A., Riley, Z.L., Sunkin, S.M., Bernard, A., Puchalski, R.B., Gage, F.H., Jones, A.R., Bajic, V.B., Hawrylycz, M.J., Lein, E.S., 2008. Genomic anatomy of the hippocampus. Neuron 60, 1010–1021.

Tonegawa, S., Liu, X., Ramirez, S., Redondo, R., 2015. Memory engram cells have come of age. Neuron 87, 918–931.

Valero, M., Cid, E., Averkin, R.G., Aguilar, J., Sanchez-Aguilera, A., Viney, T.J., Gomez-Dominguez, D., Bellistri, E., de la Prida, L.M., 2015. Determinants of different deep and superficial CA1 pyramidal cell dynamics during sharp-wave ripples. Nat. Neurosci. 18, 1281–1290.

Van Raamsdonk, J.M., Pearson, J., Slow, E.J., Hossain, S.M., Leavitt, B.R., Hayden, M.R., 2005. Cognitive dysfunction precedes neuropathology and motor abnormalities in the YAC128 mouse model of Huntington's disease. J. Neurosci. 25, 4169–4180.

van, L.H., de Haan, T.R., Offringa, M., Post, B., van der Lee, J.H., 2013. Prognostic tests in term neonates with hypoxic-ischemic encephalopathy: a systematic review. Pediatrics 131, 88–98.

Varoqueaux, F., Sigler, A., Rhee, J.S., Brose, N., Enk, C., Reim, K., Rosenmund, C., 2002. Total arrest of spontaneous and evoked synaptic transmission but normal synaptogenesis in the absence of Munc13-mediated vesicle priming. Proc. Natl. Acad. Sci. U. S. A. 99, 9037–9042.

Venerosi, A., Valanzano, A., Alleva, E., Calamandrei, G., 2001. Prenatal exposure to anti-HIV drugs: neurobehavioral effects of zidovudine (AZT) + lamivudine (3TC) treatment in mice. Teratology 63, 26–37.

Verhage, M., Maia, A.S., Plomp, J.J., Brussaard, A.B., Heeroma, J.H., Vermeer, H., Toonen, R.F., Hammer, R.E., van den Berg, T.K., Missler, M., Geuze, H.J., Sudhof, T.C., 2000. Synaptic assembly of the brain in the absence of neurotransmitter secretion. Science 287, 864–869.

Xiao, H., Liu, B., Chen, Y., Zhang, J., 2016. Learning, memory and synaptic plasticity in hippocampus in rats exposed to sevoflurane. Int. J. Dev. Neurosci. 48, 38–49.

Yamatani, H., Kawasaki, T., Mita, S., Inagaki, N., Hirata, T., 2010. Proteomics analysis of the temporal changes in axonal proteins during maturation. Dev. Neurobiol. 70, 523–537.

Yoshimura, Y., Callaway, E.M., 2005. Fine-scale specificity of cortical networks depends on inhibitory cell type and connectivity. Nat. Neurosci. 8, 1552–1559.